CIRP Journal of Manufacturing Science and Technology 58 (2025) 1–19

Contents lists available at ScienceDirect

CIRP Journal of Manufacturing Science and Technology

journal homepage: www.elsevier.com/locate/cirpj

Ultra-precision surface treatment of beta-titanium alloy printed using laser and electron beam melting sources

Jibin Boban [a,b,*], Afzaal Ahmed [a], Ozkan Gokcekaya [c], Takayoshi Nakano [c]

[a] Department of Mechanical Engineering, Indian Institute of Technology Palakkad, Kerala 678623, India
[b] Mikrotools Private Limited, Jalan Bukit Merah, 159456, Singapore
[c] Division of Materials and Manufacturing Science, Graduate School of Engineering, Osaka University, Osaka 565-0871, Japan

ARTICLE INFO

Keywords:
Additive manufacturing
Powder bed fusion
Diamond turning
Titanium
Microstructure

ABSTRACT

Additive Manufacturing (AM) is a near net shape fabrication technology offering exceptional design freedom for complex part production. However, the inadequate surface quality and poorly generated micro-features adversely affect the functional performance of metal AM parts thereby restricting the direct adoption in biomedical implantation applications. Ultra-precision diamond turning (UPDT) can be regarded as a possible solution to overcome the aforementioned challenges in metal AM. However, the machinability of metal AM parts at ultra-precision level is highly sensitive to the material specific attributes and microstructure generated by the thermal characteristics of the process. In light of this, the present study follows a novel direction by investigating the dependence of distinct material characteristics imparted by two different AM powder melting sources on the ultra-precision post-treatment performance. Experiments were conducted on laser and electron beam printed beta-Ti alloy (Ti-15Mo-5Zr-3Al) which has potential importance in biomedical applications. The results demonstrate that the microstructural variations in respective samples affect the process performance and final surface integrity. The samples printed using laser powder bed fusion (LPBF) achieved a final surface finish (Sa) of ~66.3 nm after UPDT relative to the electron beam powder bed fusion (EPBF) samples (~104.3 nm). The cutting forces tends to exhibit sharp dip in forces in case of LPBF samples when micro-cutting was done perpendicular to the beam scanning direction. The chip morphology analysis corresponding to the LPBF and EPBF samples substantiates the generation of chips with segmentation/serrations on the free chip surface and parent material adhesion on the tool-chip contact surface. Further, precise microfeature generation was successfully accomplished on both the samples with minimal dimensional deviations on LPBF sample. Thus, the outcomes of the study establish the potential of UPDT in elevating the bioimplant surface standards of beta-Ti alloy with superior performance in LPBF samples.

1. Introduction

Metal Additive Manufacturing (AM) is an advancing technology gaining momentum in the modern industrial scenario owing to its feasibility in producing complex/intricate shaped products [1]. The exceptional design freedom, mass customization flexibility and possibilities of tailoring the material properties constitute the superior benefits of metal AM over conventional manufacturing methods [2]. Further, AM offers higher efficiency in batch production [3] and ensures minimal scrap generation [4]. However, the inadequate level of surface quality, geometrical form errors, dimensional inaccuracy (deviations from acceptable tolerance limits in quality control) and higher cost of production hinder the effective implementation of metal AM components in industries [5]. The irregularities/defects present over the surface can unfavourably influence the functional performance of metal AM parts [6]. Further, the least possible limit associated with the layer thickness and laser/electron beam spot diameter in AM restricts the realization of high resolution micro-features on metals [7].

Biomedical sector largely utilizes the customization flexibility of AM technology in the production of patient-specific implants. However, as far as biomedical implant applications are concerned, the expected level of surface finish and form accuracy requirements are highly stringent [8]. Some of the biomedical implants critically demand mirror like surface finish for ensuring desired functionality [9]. For instance,

* Corresponding author at: Mikrotools Private Limited, Jalan Bukit Merah, 159456, Singapore.
E-mail address: jibin@mikrotools.com (J. Boban).

https://doi.org/10.1016/j.cirpj.2025.01.006
Received 18 October 2024; Received in revised form 21 December 2024; Accepted 15 January 2025
Available online 31 January 2025
1755-5817/

exceptional surface finish (Ra) of less than 100 nm is one of the prime requirements at part regions like bearing surfaces (hip and knee joints), where sliding action occurs [10]. Despite the functional performance, ultra-smooth finish on such surfaces can offer durability to the biomedical implants [11]. Further, surfaces with texturing or micro-features are of increasing importance in biomedical applications to control osseointegration or cell growth after implantation [12]. Therefore, the adoption of post-processing operations on metal AM parts is inevitable [13] to meet the biomedical standards. Ultra-Precision Diamond Turning (UPDT) is a reliable solution for accomplishing nanometric finish and excellent form tolerance on metallic materials [14]. UPDT technology is extensively adopted in applications such as mobile camera lenses, X-ray deflection mirrors, ophthalmic implant production, telescopic mirrors etc. [15]. Nevertheless, the potential of UPDT in enhancing the functional performance of metal AM parts has been minimally explored which forms the motivation behind the present study. Thus, the investigation evaluates the potential of ultra-precision diamond turning in enhancing the acceptability of AM components in biomedical implant applications. Further, the machinability of metallic parts at ultra-precision level is highly sensitive to the material specific attributes and microstructure generated by the thermal characteristics of the process [16]. In light of this, the present study also investigates the dependence of distinct part characteristics imparted by two different AM thermal sources, such as laser and electron beam, on the ultra-precision machinability of β-Ti alloy.

2. State-of-the-art on surface post-treatment of additively manufactured bioimplant alloy materials

SS316L, Ti6Al4V and CoCr constitute the materials generally used in bioimplant applications [17]. The upcoming subsections discuss the state-of-the-art in the surface post-treatment of such metal AM bioimplant materials from the standpoint of improvement in part quality.

2.1. Review on non-traditional surface post-treatments

Chemical finishing is one of the viable post-processing variant that can be adopted at instances when the metal AM bioimplants are complex and customized as per patient-specific requirements. The chemical polishing studies conducted by Zhang et al. [18] on additively manufactured Ti6Al4V involved erosion and levelling phases. Although the former erosion stage removed the irregularities from the surface, some stream tracks were left behind as residues. Nevertheless, the subsequent levelling process was able to eliminate such stream tracks leading to smoother surfaces. The process could also improve the corrosion resistance of Ti6Al4V owing to the formation of a thin passivation layer over the surface after chemical finishing. The adoption of chemical polishing on Titanium tissue scaffolds produced by Laser Powder Bed Fusion (LPBF) was also found successful in a later study [19]. The process resulted in homogenous polishing leading to significant enhancement in surface finish. However, considerable loss in scaffold mass was experienced after the elimination of non-melted and partially melted powder particles from the strut surface. Additionally, an increase in porosity was detected at the shell and core of the Titanium scaffold after chemical polishing. A similar study also reported that HF-HNO_3 chemical polishing leads to excess material removal or mass loss from LPBF Ti6Al4V [20]. Further, the investigations carried out on electron beam melted Ti6Al4V in another study showed that the efficiency of chemical finishing is highly sensitive to the difference in solution concentration [21]. Moreover, Sefer et al. [22] reported that chemical finishing of Ti6Al4V using HF-HNO_3 solution involves preferential dissolution of α phase relative to β phase resulting in non-uniform material removal. Thus, the selective phase dissolution in multiphase alloys [23] and difficulty in process control [24] hinders the large-scale utilization of chemical polishing strategies in practical applications.

Laser polishing is another method being investigated by researchers for enhancing the surface quality of metal AM components. Investigations of Marimuthu et al. [25] on laser polishing of LPBF Ti6Al4V samples showed a reduction in as-printed surface roughness of ~10.4 μm to ~2.4 μm (top surface). However, the polished surface exhibited repeated striations at higher laser power as a consequence of increased velocity associated with the melt pool. A similar study on LPBF SS316L samples also confirmed that excessive input of laser energy can generate cavities with microcracks on the processed surface [26]. Although sub-micron surface finish of ~0.28 μm was achieved after laser polishing on top surface in the XY plane, the evolution of surface morphology was strongly dependent on the melt pool surface tension during the process. Despite SS316L, surface finish in sub-micron range had been achieved by researchers using laser polishing on AM biomaterials like CoCr [27] and Ti alloys [28]. In another study, a prior ablative process was recommended by Gora et al. [29] to improve the efficacy of laser polishing process. The strategy yielded ~85 % improvement in surface finish on as-printed Ti6Al4V side surfaces (along Z direction) through efficient elimination of large scale surface defects/irregularities. However, laser polishing can generate significant level of tensile residual stresses ($\sigma >$ 500 MPa) on metal AM surfaces as reported in the study conducted by Tian et al. [30]. Thus, laser polishing demands the requirement of an additional stress relief heat treatment operation to minimize the tensile residual stresses thereby raising the cost of post-processing phase. Laser polishing trials using nanosecond pulses attempted by Ma et al. [31] on AM Ti6Al4V alloy showed ~32 % improvement in surface hardness owing to the formation of α' martensitic phase. However, Xu et al. [32] proved that the thermal impact of laser polishing can induce the evolution of cracks at TiAl subsurface which is detrimental to the mechanical functionality of the components. Besides the aforementioned setbacks, the polishing time required is higher for larger samples due to the small spot size associated with a laser beam thereby reducing cost effectiveness in production [33]. The limited accessibility of the laser head towards internal surfaces [34] and complex internal features also raises challenges in post-processing [35].

Taking note of such limitations, Bouland et al. [36] endeavoured Abrasive Flow Machining (AFM) experiments on LPBF Ti6Al4V parts. The abrasive medium was a mixture of boron carbide, polyborosiloxane polymer, lubricating greases and minor amounts of oleic acid. The as-printed surface roughness of ~13.97 μm was reduced to ~0.23 μm after 100 AFM passes on samples printed at 90° surface orientation. However, the study also states that the mass loss experienced in AFM can aggravate the part geometry and dimensional accuracy. Further, AFM process results in rounding of the sharp edges present on metal AM components [37]. Magnetic Abrasive Finishing (MAF) approach attempted by Zhang et al. [38] was also effective in removing the surface defects like balling and partially melted particles. The MAF operation involved 75 min of polishing time to achieve a final surface finish of ~2.85 μm on top surface (XY plane). Electric discharge assisted post-treatment is another variant recommended for achieving sub-micron surface finish on metal AM SS316L [39] and Ti6Al4V [40] parts. However, the method induces the formation of an oxygen rich resolidified layer over processed surface which may be undesirable in certain applications [41].

2.2. Review on conventional surface post-treatments

Conventional surface treatments can ensure cost-effectiveness and minimize setup complexity in post-processing phase as compared to non-conventional methods. The conventional milling operation employed on LPBF Ti6Al4V in one of the studies contributed an exceptional surface finish of ~0.3 μm [42]. Although partially melted powder particles were efficiently removed from the surface (parallel to z direction), residual milling stripes were visible all over the surface. The study also established the incompetency of micromachining and vibratory grinding processes in improving the surface finish relative to milling operation. In spite of the fact that conventional grinding excels in

imparting surface quality similar to milling, the investigations of Rakurty et al. [43] reported the development of tensile residual stresses after grinding under industrial standard flood cutting fluid conditions.

The use of heat treatment followed by sand blasting on LPBF Ti6Al4V in another study was shown to effectively remove the loosely adhered metallic particles from the as-printed lattice structures [44]. But, the particle bombardment action in sand blasting process and consequent plastic deformation can elevate the chances of pit formation on the upper surface [45]. In a later investigation conducted by Kaynak and Kitay [46], the potential of Finish Machining (FM), Vibratory Finishing (VF) and Drag Finishing (DF) was studied by considering additively fabricated SS316L round bars. FM induced enhanced integrity and hardness at the surface in contrast to other methods. However, the study pointed out that FM is restricted to simple geometrical profiles in comparison with VF and DF methods.

Further, Surface Mechanical Attrition Treatment (SMAT) was introduced by Sun et al. [47] for improving the surface quality of SLM SS316L samples. Surface finish similar to that achievable in surface grinding (Ra < 0.5 μm) was accomplished through SMAT with ~96 % reduction in roughness. The plastic deformation of partially melted particles and roughness peaks eventually filled the valleys leading to surface smoothening. Moreover, the strain hardening induced by the process elevated the surface hardness and tribological characteristics of SS316L specimens. Some of the studies demonstrated that SMAT can generate compressive residual stresses on the processed LPBF SS316L and Ti6Al4V surfaces [48]. However, the process has a saturation limit for roughness reduction as highlighted in the work of Arifvianto et al. [49]. The study also indicated that SMAT process can cause surface erosion resulting in mass reduction of the samples.

2.3. Review on processing high resolution micro-features on metal AM surfaces

Micron-scale manufacturability is an important requirement in industries and is critically challenging using metal AM technology. The research work executed by Worts et al. [50] illustrated that laser polishing is capable of generating microconical structures and nanogratings on AM Titanium parts by maintaining proper control of processing speed and pulse energy. The microconical features exhibit potential in controlling the wettability of surfaces, while the latter can be utilized as a means to encode numerical information. However, the thermal impact of laser polishing can modify the subsurface properties and induce micro-cracks over the surface. Studies on micro-AM technology are also in progress to accomplish the production of microfeatures directly on metal AM components during printing [51]. Nevertheless, the minimum resolution of features achieved till date is ~15 μm. Moreover, micro-scale AM technologies demand specialized design methodologies and experiences many constraints due to the difficulty in scaling [52]. A single layer single track strategy was put forward by Simson and Subbu [53] with an aim to produce microfeatures that can alter the surface topography for enhanced tribological performance. The size of micro-feature reported in the study had a mean height of ~40 μm and a width of ~150 to ~300 μm. In the same direction, Mekhiel et al. [54] introduced a novel additive texturing approach which facilitates tailoring of surface attributes for enhanced functionality of metal AM component. However, the minimum feature size obtained via LPBF had a width of ~100 to ~150 μm. Similarly, Dwivedi et al. [55] also attempted additive texturing with an aim to enhance the biotribological performance and wettability of SS316L additive implants. The minimum diameter of dimple/groove considered in the study was also ~150 μm.

Wei et al. [56] proposed an Electrolyte Column Localized Electrochemical Deposition (ECL-ECD) method for printing micron-sized features on metal AM components. The process involves localized electro-deposition of metal by the electrolyte column maintained between cathodic surface and electrolyte nozzle (anode). The easiness in nozzle motion control favours the production of 3D intricate microfeatures with a surface roughness (Sa) of ~0.2 μm. Nonetheless, the nozzle diameter considered in the study was 240 μm which contributed to a feature size ranging between ~180 μm and ~200 μm. Table 1 provides a concise overview of aforedescribed research works related to post-treatment of metal AM parts.

From the state-of-the-art, it is apparent that the established surface post-treatment operations experience many challenges in improving the surface integrity and functional performance of metal AM bioimplant materials. Additionally, the best surface finish achievable using most of the methods is restricted up to only sub-micron level. Further, the ineffectiveness of metal AM technology in accomplishing microfeatures of high resolution raises the strong requirement of a process capable of producing nanofinished surfaces and high resolution microfeatures. UPDT is an advanced technique implemented for achieving nano-level surface finish in optical applications [14]. The modern multi-axis UPDT machines have extended capabilities for machining freeform surfaces relative to conventional turning machines [57]. Further, with proper tool path generation, certain degree of complex/ intricate profiles can also be cut using diamond turning implying its feasibility in the post-treatment of metal AM parts [58]. Therefore, the present study investigates the potential of a hybrid approach merging powder bed fusion (PBF) with UPDT for enhancing the acceptability of metal AM alloys in biomedical implant applications. Further, the past studies elucidate that a comprehensive research focussing on microstructural variations induced by distinct AM thermal sources and corresponding influence on post-processing performance is limited. Thus, the study focusses on an AM alloy printed using both laser and electron beam thermal sources to understand the respective effect on ultra-precision machinability performance.

The state-of-the-art also discloses that the studies on post-treatment of AM biomedical alloys are more concentrated on Ti alloys, specifically on Ti6Al4V material. Although Ti6Al4V ensures good biocompatibility, the substantial presence of aluminium and vanadium can be toxic to the body as it can trigger certain allergic reactions [59]. Moreover, the considerable mismatch between the Young's modulus of Ti6Al4V (~110 GPa) and the surrounding bone (~10–30 GPa) can induce stress shielding effect in implants [60]. Ti-15Mo-5Zr-3Al is a metastable β -Ti alloy widely adopted in bioimplant applications due to its less toxic behaviour with the young's modulus value closer to that of human bones (~44 GPa) [61]. Moreover, β-Ti alloys can offer excellent biocompatibility, good corrosion resistance and appreciable specific strength demanded by biomedical implants [62]. Therefore, Ti-15Mo-5Zr-3Al is taken into consideration as the AM alloy material in the present investigation.

3. Experimental procedure

The details of material and methods used for the fabrication of metal AM samples are discussed in the present section. The specifications related to energy source, powder material attributes and process parameters fixed in each AM method (LPBF and EPBF) are elucidated. The section also explains the ultra-precision micro-cutting approach used in the study. The characterization equipment/devices used for the present study is also detailed in the last subsection.

3.1. Material and experimental details

Ti-15Mo-5Zr-3Al powder material was used for fabricating the metallic AM samples. The chemical composition of Ti-15Mo-5Zr-3Al material employed for PBF fabrication is provided in Table 2. LPBF samples for the investigations were printed using an LPBF machine (Model: EOS M290). The equipment comprises of an Ytterbium (Yb) fiber laser having wavelength in the range of 1060 to 1110 nm with maximum output power of 400 W. The size of powder material particle chosen for printing lies in the range of ~ 18–44 μm with a mean diameter of ~30 μm. The EPBF powder particles had a mean diameter of

Table 1
Concise overview of past literature.

SI No.	Reference	Year	AM method	Roughness of AM part	Material	Strategy for part quality improvement	Surface finish after post-treatment	Challenges/Limitations
1.	Scherillo et al.	2020	EBM	Sa = ~37.5 μm	Ti6Al4V	Chemical polishing	Sa = ~1.8 μm	Efficiency is sensitive to solution concentration
2.	Wyzocki et al.	2019	LPBF	-	Ti	Chemical polishing	-	Loss in scaffold mass and increase in porosity
4.	Marimuthu et al.	2015	LPBF	Ra = ~10.2 μm	Ti6Al4V	Laser polishing	Ra = ~2.4 μm	Striations on polished surface at high laser power
5.	Li et al.	2023	LPBF	Sa = ~7.02 μm	SS316L	Laser polishing	Sa = ~0.38 μm	Cavity formation with microcracks at excess laser energy
6.	Tian et al.	2018	LPBF	Sa = ~21.46 μm	Ti6Al4V	Laser polishing	Sa = ~5.5 μm	Tensile residual stresses at processed surface
7.	Xu et al.	2021	LDM	Ra = ~16.06 μm	TiAl	Laser polishing	Ra = ~1.76 μm	Crack evolution at subsurface
8.	Bouland et al.	2019	LPBF	Ra = ~13.97 μm	Ti6Al4V	Abrasive flow machining	Ra = ~0.22 μm	Geometrical inaccuracy arising from mass loss
9.	Boban et al.	2022	LPBF	Sa = ~9.32 μm	Ti6Al4V	Electrical discharge polishing	Sa = ~0.84 μm	Oxygen rich resolidified layer on surface
10.	Bagehorn et al.	2017	LPBF	Ra = ~17.9 μm	Ti6Al4V	Milling	Ra = ~0.3 μm	Milling stripes over the surface
11.	Rakurty et al.	2023	EPBF	-	Ti6Al4V	Grinding	Ra = 1 to 2 μm	Tensile residual stresses at processed surface
12.	Kaynak and Kitay	2019	LPBF	Ra = ~7 μm	SS316L	Finish machining (Turning)	Ra = ~1.7 μm	Process restricted to simple geometrical profiles
13.	Mekhiel et al.	2021	LPBF	Ra = ~14.5 μm	SS316L	Additive texturing	-	Minimum feature width limited to ~100 to ~150 μm

Table 2
Chemical composition of Ti-15Mo-5Zr-3Al powder.

Element	Ti	Mo	Zr	Al	O
Weight %	Balance	15	5	3	0.15

~ 70 μm with sizes ranging from ~44–100 μm. The samples corresponding to EPBF were printed via an electron beam printing equipment (Model: Arcam, Q10) having an output power of ~3.5 kW.

Specimens with a square cross section of 10 mm (b) × 10 mm (w) × 50 mm (l) printed using LPBF and EPBF were used for the investigation. Both vertically (along Z) and horizontally (along Y) oriented samples were built on top of a base plate aligned in XY plane. The samples were printed using alternating X scan strategy where the beam scanning is executed parallel to the X direction. Although scan rotation is recommended during printing, X scan strategy is adopted in the present investigation instead of rotation to clearly understand the microstructural evolution in the samples during part building. The schematic representation of LPBF and EPBF fabrication of the β-Ti alloy samples is shown in Fig. 1.

The process parameter settings used in the fabrication of LPBF and EPBF samples are provided in Table 3. The process parameters for LPBF and EPBF chosen in the study could contribute sufficient relative density to the samples after printing indicating negligible porosity and lack of fusion defects. This was important to yield reliable results as it

Table 3
Process parameters used in LPBF and EPBF of Ti-15Mo-5Zr-3Al alloy.

AM method	Energy source power (W)	Layer thickness (μm)	Scanning speed (mm/s)	Hatch spacing (μm)
LPBF	320	60	900	70
EPBF	1200	60	9000	100

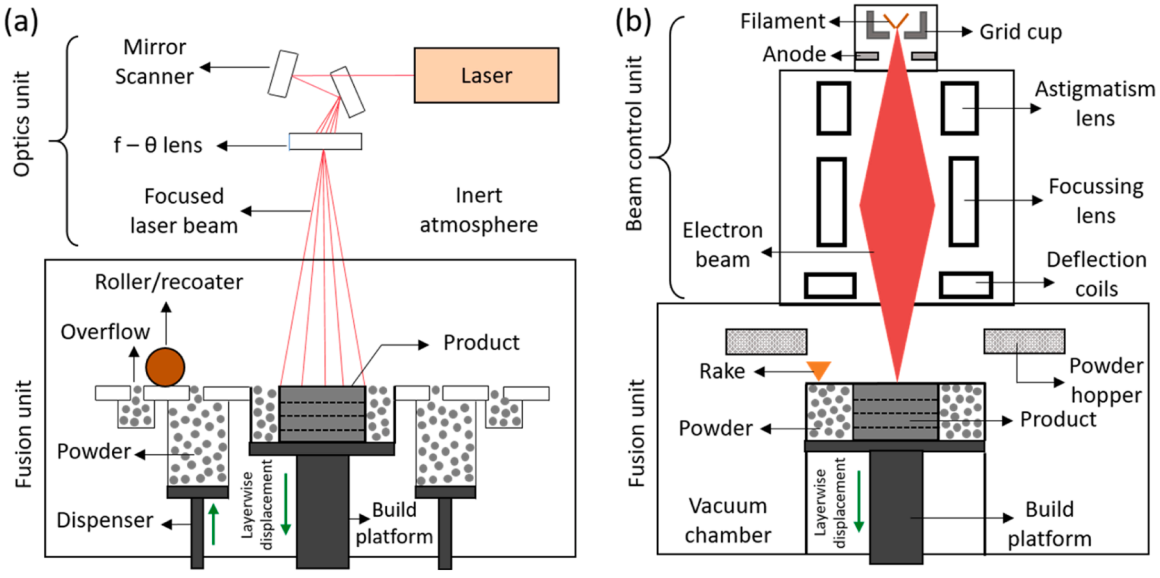

Fig. 1. Schematic depicting (a) LPBF and (b) EPBF fabrication of Ti-15Mo-5Zr-3Al alloy. Laser beam is directed towards the metallic powder region to melt and fuse each powder layer in LPBF process based on CAD design. In contrast, electron beam is used to selectively melt the regions of powder bed in vacuum atmosphere.

suppresses the influence of defects on UPDT performance. The energy density maintained during the printing of EPBF samples were nearly 3 to 4 times lesser compared to LPBF samples. The reason can be attributed to the high preheating temperature maintained in EPBF system which minimizes the net energy requirement for melting the powder. Thus, the actual energy density required for powder material fusion remains more or less same for both the samples. In order to minimize oxidation and attain denser parts, Argon atmosphere was adopted during LPBF process, whereas vacuum was maintained in the build chamber during EPBF.

3.2. UPDT experimentation and conditions

The ultra-precision micro-cutting experiments were executed on an advanced diamond turning lathe machine (Model: Optima 100, Mikrotools) as shown in Fig. 2(a). The diamond turning machine comprises of an aerostatic spindle having high axial and radial stiffness. Moreover, the hydrostatic guideways in the equipment ensure excellent precision control and accuracy in X and Z axis.

The experiments were conducted using a polycrystalline diamond cutting (PCD) tool (Fig. 2(b)) which had a rake angle of 0° and nose radius of 400 μm. The tip of the diamond tool was centred relative to the β-Ti alloy workpiece axis prior to micro-cutting experiments. The three dimensional schematic of the microgroove cutting procedure is illustrated in Fig. 2(c). The numerical G-code inputs were loaded in the graphical user interface (GUI) to accomplish the desired axis movements in terms of tool-workpiece motion.

Facing operation was carried out on LPBF and EPBF samples at optimum level of parameter settings (determined using pilot experiments) that yielded superior surface finish (spindle speed of 1000 rpm, depth of cut of 2 μm and feed rate of 0.1 mm/min). Followed by the facing operation, micro-groove cutting tests were conducted at distinct settings of cutting speed and depth of cut. The methodology adopted for the experiments is schematically represented in Fig. 3(a).

As shown in Fig. 3(b), the micro-cutting experiments were executed in directions parallel and perpendicular to energy source scanning direction. The distinct process parameter settings in micro-cutting tests were selected to be in accordance with the parameter ranges considered in past literature for force measurement and chip analysis. Machining force signals were also acquired in parallel during micro-cutting trials. The chips arising from micro-groove cutting were collected for each experiments to study the morphological attributes. The experimental details along with the conditions are provided in Table 4.

3.3. Characterization

A white light interference optical profilometer (Model: Nanomap 1000 WLI, AEP Technology) was utilized to examine the surface topography and surface roughness of the fabricated and processed PBF samples. The hardness measurements associated with the components in as-built condition were accomplished using a universal hardness tester (Model: 251 VRSA, AFFRI). Further, a sophisticated Field Emission Scanning Electron Microscope (FESEM) was utilized in order to capture the SEM images and EDS spectrum related to the investigation (Model: Gemini 300, Carl Zeiss). Electron Back Scatter Diffraction (EBSD) measurements were conducted using a different FESEM equipment (Model: JIB-4610F, JEOL) equipped with EBSD detector (Model: Aztec HKL, Oxford Instruments). The microstructural images were taken with the support of a metallurgical microscope (Model: Suxma series, Conation Technologies). The XRD patterns corresponding to the PBF samples were captured using the assistance of an X-Ray diffractometer (Model: Smartlab, Rigaku). Raman spectra was recorded using a Raman spectrometer equipped with a confocal microscope (Model: Labram HR Evo, Horiba). The PCD tool is fixed inside a tool holder firmly. The tool holder was mounted over an 8-channel dynamometer (Model: 9119AA2, Kistler) to acquire the machining force data during micro-cutting experiments. Fig. 4 illustrates the flowchart outlining the methodology employed in the present research work.

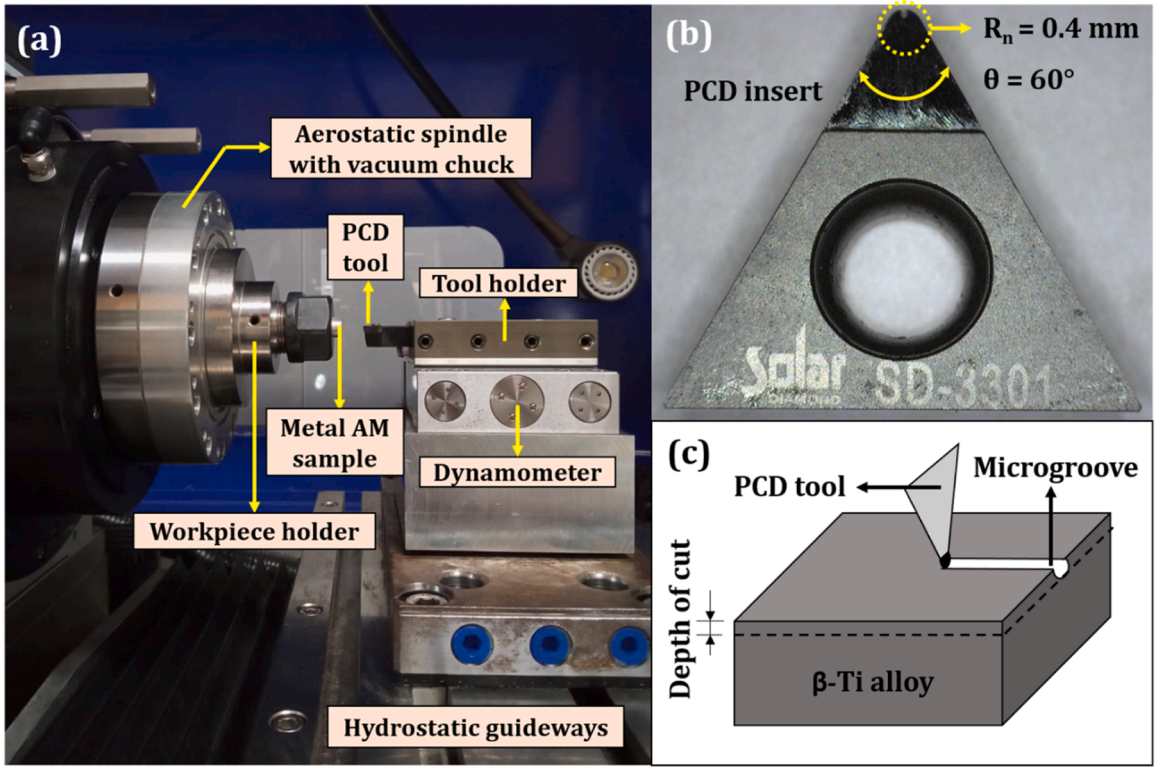

Fig. 2. (a) Experimental apparatus showing metal AM sample fixed on vacuum chuck and a PCD tool mounted on a dynamometer, (b) PCD tool insert having a nose radius of 400 μm and an included angle of 60° and (c) 3D schematic of microgroove linearly along metal AM sample surface cutting using PCD tool.

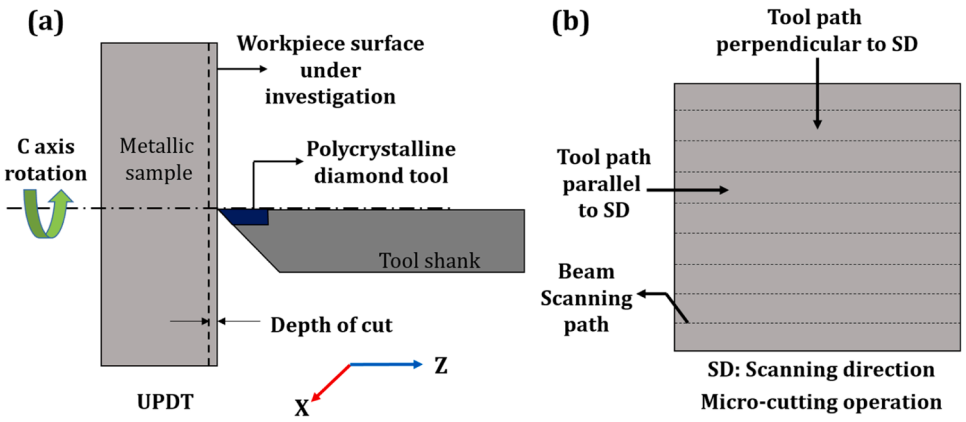

Fig. 3. Schematic representation of (a) ultra-precision diamond turning and (b) micro-cutting methodology. The polycrystalline diamond (PCD) tool is aligned with the centre of the metal AM sample and relative motion is controlled in X, Y and rotational C axis during facing operation.

Table 4
Experimental details and conditions.

Parameters	Conditions
Spindle air pressure (bar)	6.5
Hydraulic oil pressure (bar)	32
Cutting tool	Polycrystalline diamond (PCD)
Tool rake angle (deg)	0
Tool nose radius (μm)	400
Cutting speed (mm/min)	25, 50, 75, 100
Depth of cut (μm)	2, 4, 6, 8, 10

4. Results and discussions

The major results obtained from the investigation and related discussions based on detailed characterization are provided in the upcoming sections.

4.1. Surface integrity analysis

The surface integrity achieved by PBF samples after UPDT is examined by analysing the surface morphology and measuring surface roughness corresponding to the samples.

4.1.1. Surface morphology

The surface morphology related to Ti-15Mo-5Zr-3Al alloy built using LPBF and EPBF methods is represented in Fig. 5. As evident from Fig. 5 (a), the top surface of LPBF Ti alloy is characterized by the presence of well-defined scan tracks which are nearly parallel to each other. The boundary of each scan track is well defined due to the clear tracing and sharp melting by the laser beam. Fig. 5(c) shows the melt traces visible after laser beam scanning. The existence of non-melted particles of powder material and spattered powder residues can be clearly observed over LPBF surface. Non-melted particles arise from the lack of laser energy input during beam scanning at some regions which hinders sufficient melting of powder material. Similarly, the combined effect of

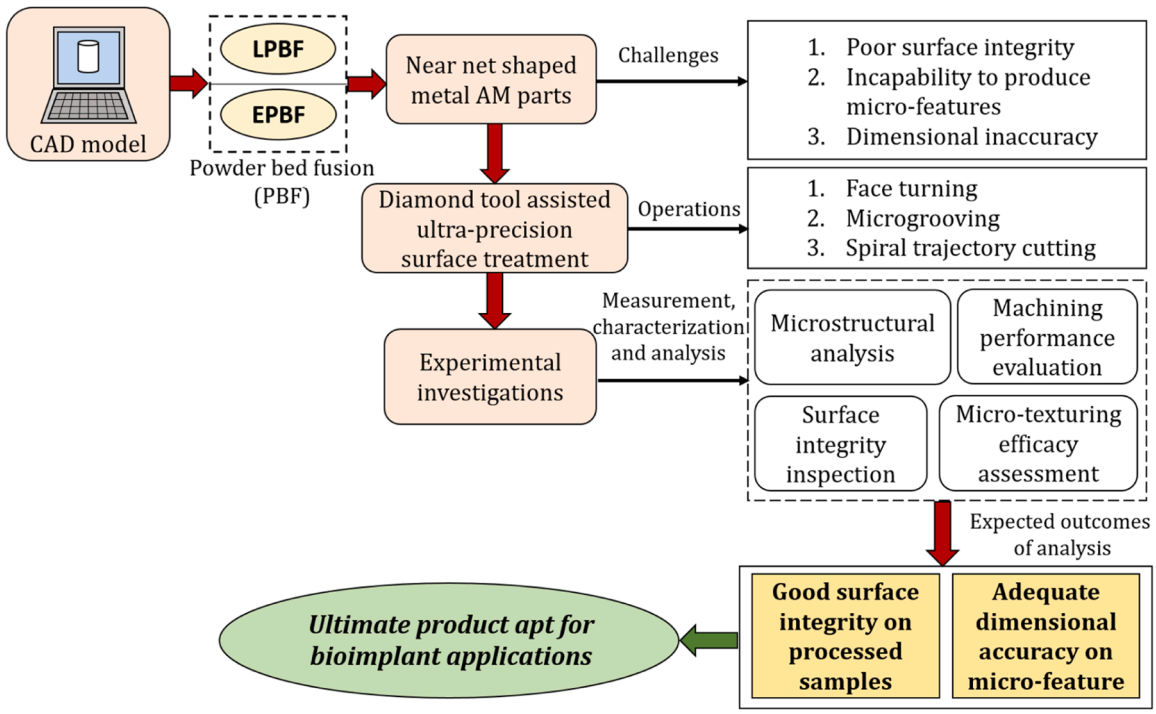

Fig. 4. Flowchart illustrating the methodology adopted in the research.

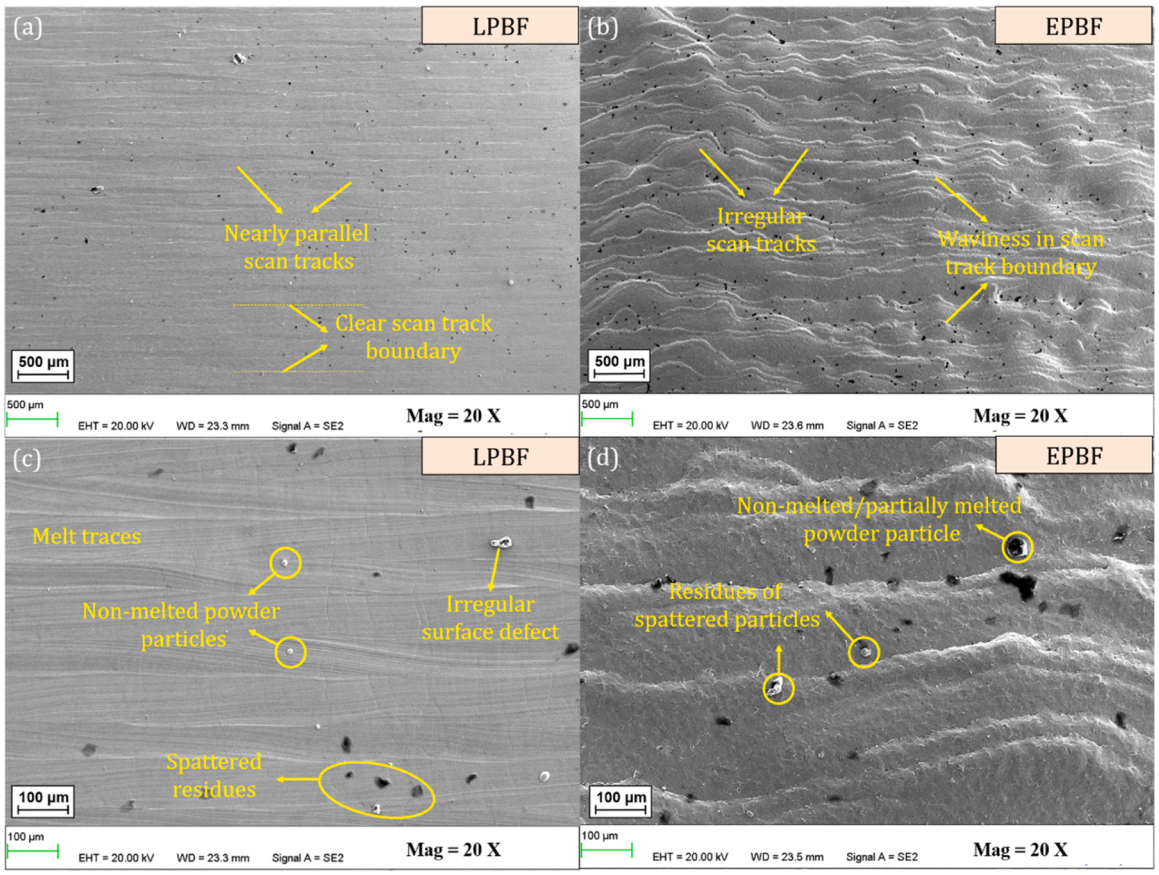

Fig. 5. Surface morphology corresponding to top surfaces of (a,c) LPBF and (b,d) EPBF Ti alloys with nearly parallel and irregular scan tracks respectively.

recoil pressure and Marangoni effect leads to spattering during PBF. In addition, the surface consists of some irregular surface defects spread over the melt traces.

In contrast, EPBF Ti alloy surface is featured by irregular scan tracks which are not parallel at most of the zones (Fig. 5(b)). The scan track boundary exhibit a wavy profile owing to the non-uniform material flow during EPBF process. Due to the preheating involved in EPBF, less amount of additional energy is required to melt the material. Thus, the temperature gradient existing in EPBF process is less which allows higher solidification/cooling time relative to LPBF. Thus, the melted material will get sufficient time to flow and spread outside the beam zone resulting in non-linear scan tracks. The melted material flow also causes partial merging of the scan track with the neighbouring track. Thus, clearly defined scan track boundaries are not evident in EPBF samples. Further, the faster scanning in EPBF leads to the formation of non-melted/partially melted particles and spattered powder residues over alloy surfaces similar to LPBF samples as shown in Fig. 5(d).

On the other side, the processing of PBF samples using UPDT (facing operation) contributed a smooth surface free from characteristic profiles obtained using the respective thermal sources (Fig. 6(a,b)). The LPBF melt traces and wavy profile of EPBF scan tracks are eliminated after UPDT. Moreover, the surface irregularities like non-melted particles and spattered powder residues were efficiently removed from the Ti alloy surfaces in both cases. However, EPBF surface still consisted of some residual particles left behind after UPDT (Fig. 6(b) in comparison with LPBF surface. Such defects correspond mainly to the chip fragments that

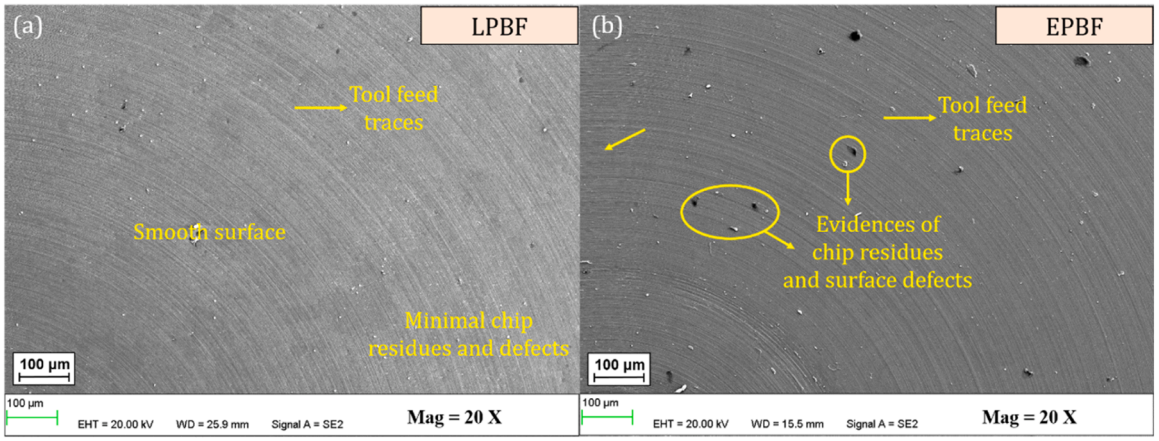

Fig. 6. Morphology corresponding to (a) LPBF and (b) EPBF Ti alloy surfaces after ultra-precision diamond turning (UPDT).

get adhered on the processed surface during UPDT. Traces of tool feed motion are also legible in both LPBF and EPBF samples after UPDT. As β-Ti alloys are characterized by lower elastic modulus, the material exhibits poor machinability. In consequence, the cutting motion leaves behind visible tool feed traces on processed surfaces.

4.1.2. Surface roughness analysis

Surface roughness corresponding to LPBF and EPBF alloy surfaces after UPDT was evaluated to assess the effectiveness of UPDT process. Surface roughness (Sa) was measured at 5 different zones of machined area for each samples. From the topographical images provided in Fig. 7 (a,b), it can be observed that the surface roughness in as-printed condition associated with EPBF samples (Sa = ~4.73 μm) is higher than the LPBF samples (Sa = ~1.34 μm). The uneven and wavy beam scanning tracks in EPBF is responsible for the increased roughness relative to LPBF samples. In addition, the larger size of powder particles in EPBF process elevates the roughness magnitude relative to LPBF process.

However, the implementation of UPDT process with multiple passes of PCD tool yielded a smooth surface with nano-level finish as evident from Fig. 8(a,b). The final finish achieved after UPDT were distinct for each samples with LPBF samples having comparatively better surface finish. As shown in Fig. 7, the final surface finish (Sa) obtained corresponding to LPBF and EPBF samples were ~66.3 nm and ~104.3 nm respectively. The difference in roughness can be attributed to the variation in the material specific properties of the samples. Moreover, the relative variation in the frequency of peaks/valleys associated EPBF roughness profiles is in agreement with the initial wavy and uneven nature of the as-printed surface.

4.2. Metallurgical properties

The analysis details of hardness values with regard to LPBF and EPBF samples is discussed in this section. Moreover, XRD analysis is carried out to determine the phases present in the fabricated samples.

4.2.1. Hardness analysis

The hardness of the samples were examined at the surfaces through Vickers test with the assistance of a universal hardness tester. Indentations were made at 5 different points on the polished surface of both LPBF and EPBF samples. The diagonals of respective indentations were measured using an integrated optical microscope and software interface. Each indentations during hardness test was carried out by selecting a load of 4.905 N (0.5 kgf) and a dwell time of 10 s. As visible from Fig. 9, the hardness value is slightly higher for EPBF samples as compared to LPBF samples. The former has a hardness value of ~344 HV, whereas EPBF samples possess a hardness of ~365 HV. The reason can be attributed to the changes in heating and cooling cycles involved in both processes that imparts metallurgical changes in the samples. The increased hardness confirms the difference in machinability of both samples and corroborates the variation in surface finish as discussed in Section 4.1.2. In light of the varied hardness associated with the samples, the phase composition of LPBF and EPBF samples were assessed using an X-Ray diffraction (XRD) analysis.

4.2.2. XRD analysis

X-Ray Diffraction (XRD) analysis was conducted with the aid of an X-ray diffractometer to determine the changes in as-printed sample phase composition arising from LPBF and EPBF processes. The radiation source adopted for attaining Bragg peaks and diffraction measurements was Cu-Kα source which has a wavelength of 1.54 Å. Continuous scanning was performed by the X-ray detector on the manually polished PBF samples to record the XRD pattern. The detector executed scanning at a speed of 3°/min from 20° to 100° by maintaining a step-width setting of 0.02°. The XRD peaks indicate that the primary phase present in both LPBF and EPBF samples was β-phase which matches with the typical phases present in Ti-15Mo-5Zr-3Al. As evident from Fig. 10, the benchmark reference peaks of β-phase matched well with the XRD pattern obtained for both the specimens. However, the XRD pattern of EPBF samples highlighted the presence of α-phase peaks in addition to β-phase (Fig. 9).

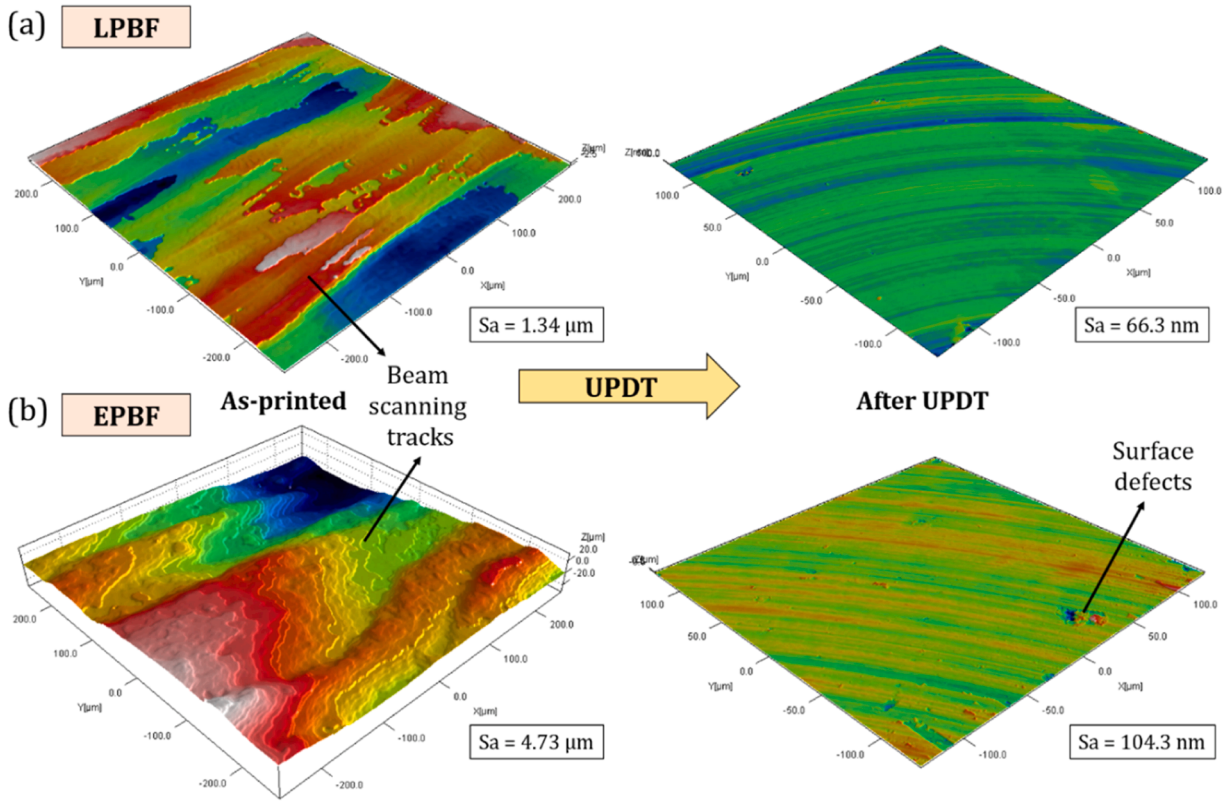

Fig. 7. Surface topography of as-printed (a) LPBF and (b) EPBF Ti alloy top surfaces.

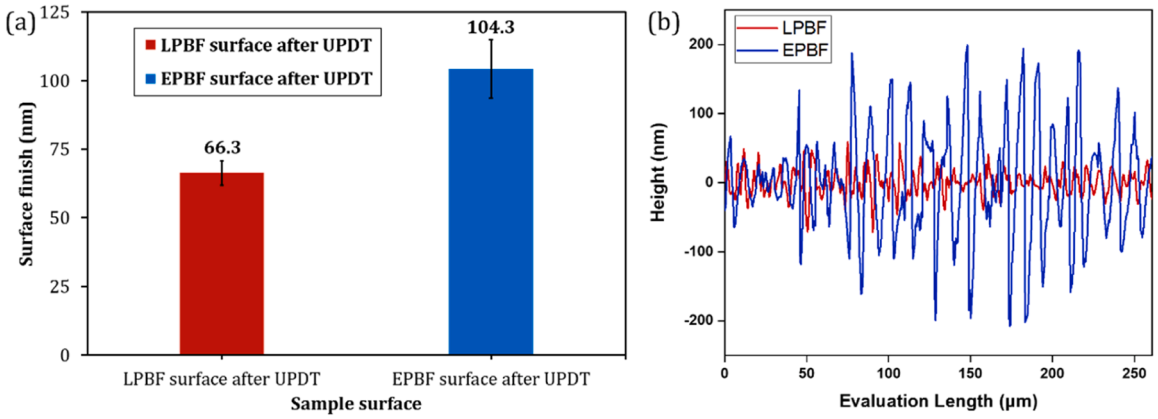

Fig. 8. (a) Surface finish achieved by LPBF and EPBF samples after UPDT and (b) the roughness profiles acquired corresponding to each samples after UPDT.

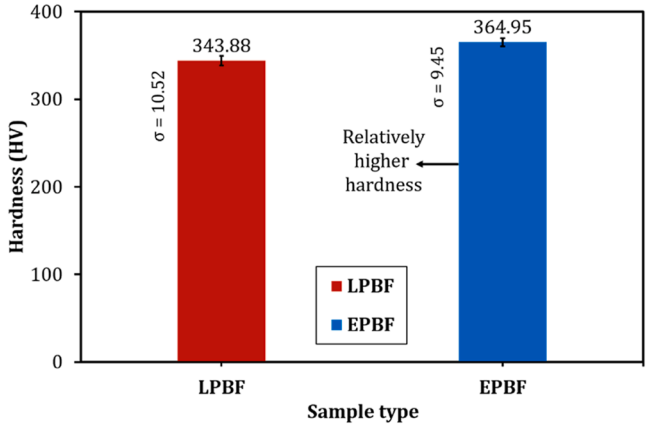

Fig. 9. Hardness of as-printed (a) LPBF and (b) EPBF Ti alloy samples taken at top surfaces.

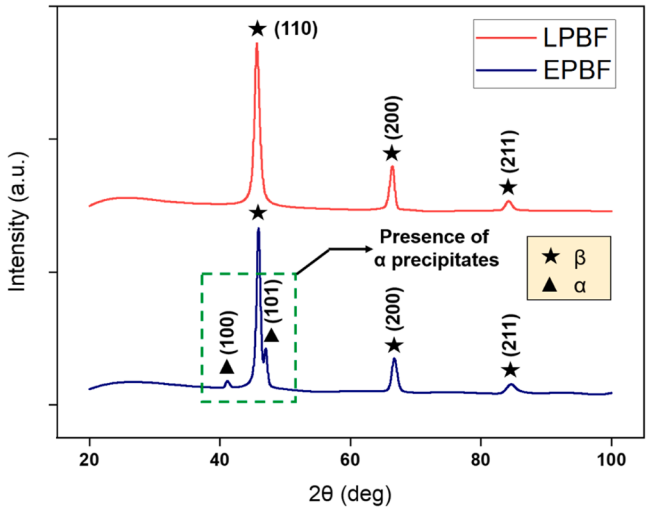

Fig. 10. XRD profiles obtained corresponding to LPBF and EPBF Ti-15Mo-5Zr-3Al alloy samples (Diffraction measurements taken using Cu-kα source at a scanning speed of 3°/min and a step width setting of 0.02°).

Similar peaks of α-phase have been reported for β-Ti alloys in previous studies by some researchers [63]. The α-phase formation in β-Ti alloy occurs on account of the difference in thermal gradient existing during EPBF process in comparison with LPBF process.

Microscopic and FESEM analysis were conducted to determine the existence of α-phase in EPBF alloy. From the optical microscopic image provided in Fig. 11 (a), α-phase precipitation can be observed at some regions in the form of lamellar colony structures. The high magnification FESEM image shown in Fig. 11 (b) establishes that the α-phase exits as plate-like precipitates in the sample. Thus, the optical microscopic and FESEM images corroborates the α-phase precipitation as obtained from XRD analysis.

During EPBF, a lower thermal gradient exists in EPBF owing to preheating of the Ti alloy powder. Preheating is enabled to elevate the electrical conductivity of the metallic powder material which in turn minimize the accumulation of charges by the electrons. The preheating lowers the effective cooling rate during the process due to lower thermal gradient and provides sufficient time for the precipitation to occur in the EPBF samples. Thus, plate-like α precipitates are formed in EPBF samples giving rise to slightly higher hardness [64] than LPBF samples.

Preheating can also lower the thermal residual stresses in EPBF samples due to the reduced thermal gradient and cooling rates relative to LPBF process [65]. However, in LPBF, only the substrate and initial build layers are subjected to preheating at mild temperature (~130 °C). Hence, high temperature gradients are developed in LPBF samples leading to rapid cooling/solidification and subsequent development of thermal residual stresses. UPDT is a post-treatment option which focusses on removing only a very thin rough material at the sample surface without impacting the bulk material. Thus, the residual stress conditions in the bulk as-printed material remain unaffected even after post-treatment.

4.3. *Effect of AM process induced microstructure*

UPDT involves remarkably fine depth of cuts in micron range. Similarly, AM attributes like layer thickness, hatch spacing, scan track width etc. also spans in microscopic scales. Thus, the microstructure in as-printed condition can play a crucial role in deciding the machining performance. Therefore, the microstructural aspects related to top and side surfaces of PBF samples are analysed and discussed in this section. The scan track profiles and grain growth attributes are evaluated in each of the PBF samples.

4.3.1. *Microstructural analysis*

The microstructure related to LPBF and EPBF samples were studied with the support of a metallurgical microscope. Both the specimen top surfaces were polished with different grades of SiC paper followed by fine polishing using colloidal Silica solution. Subsequently, the polished surfaces were etched using Kroll's reagent (90 mL H_20 + 8 mL HNO_3 + 2 mL HF) recommended for Ti alloys. The EBSD images of side surfaces were also acquired under an accelerating voltage of 20 kV and a step interval of 2 μm to confirm the arrangement and type of grains along the

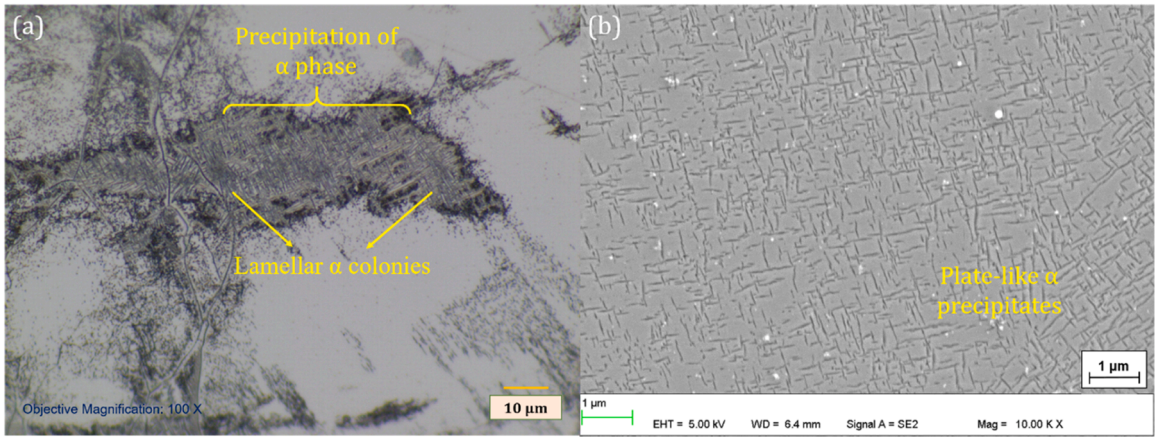

Fig. 11. High magnification (a) optical and (b) FESEM microstructural images taken on etched EPBF Ti alloy at 10 µm scale and 1 µm scale settings respectively.

depth.

From Fig. 12 (a), laser beam scanning tracks with clearly defined boundaries are clearly visible and are aligned parallel in the X-scan direction. The EBSD Inverse Pole Figure (IPF) map (Fig. 12 (c)) represents the grains on YZ surface and their orientation towards the build direction. The IPF map highlights that the melt pools and corresponding grains are stacked in the region between two consecutive scan tracks. Thus, the scan track borders evident over top surface extend downwards along the depth of the built samples. The grain orientation is identified as < 101 > oriented at the machining surface. The overlapping of melt pools resulting from penetration of laser energy towards the subsequent layers underneath is also apparent from the EBSD image.

The close observation within the scan tracks reveal the grain growth occurred in the samples as a part of PBF process. Zone 1 and Zone 2 marked in Fig. 12 (b) represent the distinct morphology of grain growth experienced in the process. The high magnification microscopic images corresponding to Zone 1 and Zone 2 signify the grain growth occurring in different orientations. These correspond to the EBSD observations on the YZ plane demonstrating various grain orientations which indicate differences in cellular growth direction. While Zone 1 represents an inclined cellular substructure (Fig. 13 (a)), Zone 2 highlights a parallel cellular substructure (Fig. 13 (b)) in the cellular network. However, the images signify that the grain growth direction is oriented towards the movement of laser scanning source. The alignment of grain growth

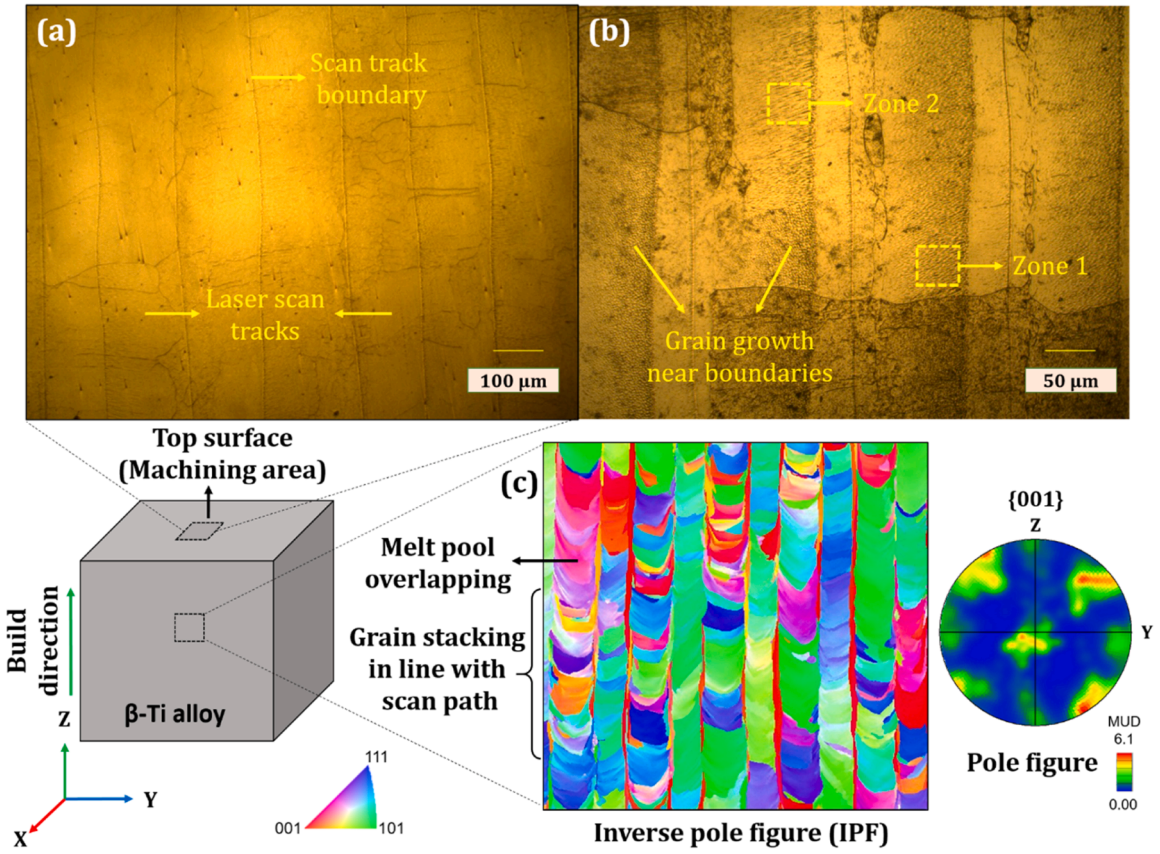

Fig. 12. Microstructure of as-printed LPBF Ti alloy surface representing (a) scan tracks, (b) grain growth and (c) EBSD image corresponding to the surface parallel to build direction.

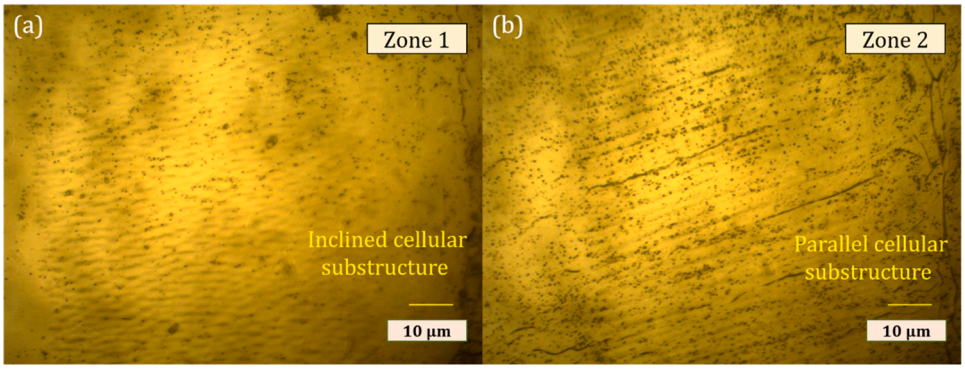

Fig. 13. (a) Inclined and (b) parallel cellular substructures observed at different zones within LPBF scan tracks.

direction occurs towards the larger thermal gradient induced by the higher intensity of laser beam experienced at the middle of the scan track.

On the contrary, the microstructure of EPBF sample shown in Fig. 14 (a) portrays the presence of non-linear scan-tracks resembling the surface morphology observations discussed in Section 4.1.1. The controlled etching of the specimen exposed the morphology of grains present in the sample. The grain morphology shown in Fig. 14 (b) shows the appearance of grains separated by boundaries within the electron beam scanning tracks. The reason behind the formation of grain structure can be attributed to the lesser thermal gradient and lower solidification rate associated with the EPBF process. Thus, adequate time is available for the development and formation of independent grains. EBSD image (IPF map) taken on side surface (Fig. 14 (c)) confirm that columnar grains and several small sized grains are developed at different regions in EPBF samples unlike the scan track boundary confined grain stacking in LPBF samples. The columnar grains are aligned vertically along the build direction. Moreover, the grain orientation at the machining surface (XY plane) is identified as $< 100 >$. Thus, the difference in microstructural aspects of LPBF and EPBF samples can affect the machinability performance in UPDT.

4.3.2. *Machining force analysis*

Micro-groove cutting experiments were conducted to assess the cutting forces in UPDT of LPBF and EPBF samples. The cutting operation was carried out in directions parallel and perpendicular to beam scanning direction of the respective thermal sources. The forces were measured using a high resolution dynamometer. The sensitivity of dynamometer in the cutting and thrust force directions was fixed to be −26 pC/N. The acquisition of cutting force signals was accomplished by

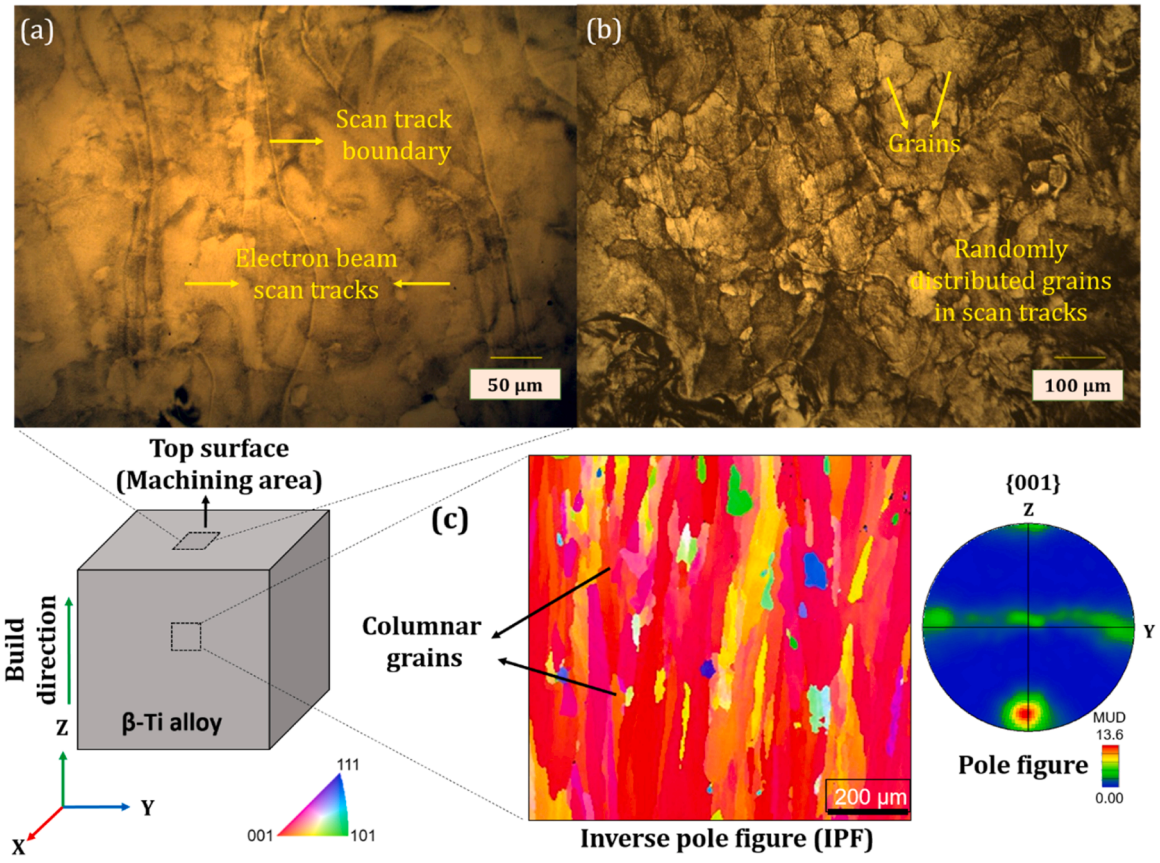

Fig. 14. Microstructure of as-printed EPBF Ti alloy surface representing (a) scan tracks, (b) grain distribution and (b) EBSD image corresponding to the surface parallel to build direction.

setting the recording frequency at 50 kHz to ensure the precise detection of force variations. The cutting velocity (v_c) and depth-of-cut (doc) for micro-cutting experiments was selected as 10 mm/min and 10 μm respectively.

From Fig. 15 (a), sharp dip in cutting forces can be noticed with respect to the mean force line during micro-cutting of LPBF samples in the direction perpendicular to beam Scanning Direction (SD) relative to parallel cutting. The reason can be attributed to the intermittent interaction of the cutting tool with scan track regions (embedded with grains) and scan track boundaries. The transition movement of the cutting tool from scan track region to scan track boundary zone leads to the abrupt dip in forces experienced during the micro-groove cutting operation. In contrast, sharp fluctuations in forces are negligible in the direction parallel to scan tracks owing to the absence of interaction with scan-track boundaries. Thus, the typical microstructure derived from LPBF process affects the UPDT performance of the samples while machining on top surfaces. However, the effect of micro-cutting perpendicular to SD is not relevant in case of EPBF samples as apparent from Fig. 15 (b). The grains evolved with well-defined boundaries dominate the effect of scan track boundaries in EPBF samples and accordingly causes random fluctuations in force signals owing to the interaction with grain boundaries.

The variation in cutting forces with respect to depth of cut and cutting speed in micro-cutting was evaluated for LPBF and EPBF Ti alloy samples. Fig. 16 (a) reveals that the cutting forces tend to rise with the increase in depth of cut for both the samples. With the increase in depth of cutting, the contact area of cutting tool with the workpiece increases leading to rise in cutting forces. At lower cutting depth, EPBF samples exhibit higher cutting forces in contrast with LPBF samples. The reason can be explained by the relatively higher hardness associated with EPBF samples. However, at increased depth of cut, the influence of dislocation density become more significant in deciding the cutting forces. LPBF samples are characterized by higher dislocation density owing to the complex thermal cycle involving faster cooling rates associated with the process [66]. The Geometrically Necessary Dislocation (GND) maps and GND plot (Fig. 17 (a, b)) derived from EBSD data for side surfaces further substantiates that GND is higher in LPBF samples indicating high ratio of dislocation due to residual stresses resulting from faster cooling rates. Contrarily, GND related to EPBF samples is relatively lower owing to the higher preheat temperature (540 °C). The average GND associated with LPBF and EPBF samples were found to be 0.64 and 0.38 respectively. Thus, GNDs form barriers to suppress plastic deformation [67] and this effect become more dominant with the increase in depth of cut. Consequently, LPBF cutting forces tend to approach EPBF cutting forces at higher cutting depths.

As evident from Fig. 16 (b), the effect of cutting speed is negligible for both LPBF and EPBF samples. Nevertheless, cutting forces exhibit a marginal rise at lower cutting speeds for both samples. The reason can be attributed to the slightly higher friction experienced at tool-chip interface in case of lower cutting speeds on account of the prolonged contact time existing during tool-workpiece interaction. With further increase in cutting speeds, the cutting forces tend to remain nearly constant for both samples.

4.4. Microgroove and chip analysis

The characteristics of microgroove surfaces formed on LPBF and EPBF samples after microcutting experiments were studied using FESEM and EDS analysis. In addition, the chips produced as a consequence of microgroove formation in both cases were analysed by considering the free surface and tool-chip contact surfaces.

4.4.1. Analysis of microgroove surface

The microgroove morphology was assessed by capturing FESEM images over the cut microgrooves. As shown in Fig. 18 (a,b), the microgroove surfaces of both LPBF and EPBF samples exhibit sliding marks aligned in parallel to the cut direction. The sliding marks arise due to the typical tool edge waviness profile associated with the PCD tool. It is worthy to note that the parallel line protrusions visible over the microgroove is featured by the presence of material protrusions having white colour in appearance produced during deformation. White coloured traces are visible on both LPBF and EPBF samples. Spot EDS was conducted to determine the elemental composition on such white spots and regions without white spots.

The points with and without white spots are indicated as 1, 2, 3 and 4, 5, 6 respectively. Spot EDS results corresponding to the microgroove cut on LPBF samples (Fig. 19 (a)) indicate slight probability of oxygen at point 2 belonging to the white spot region. The associated EDS spectra highlighting oxygen element is shown in Fig. 19 (b). Conversely, the parent material spots represented by 4, 5, 6 does not exhibit any traces of oxygen as shown in Fig. 19 (c).

Similar results are observed in case of EPBF samples (Fig. 20 (a)) where all the white spots (1, 2, 3) are featured by the indication of oxygen in minimal amounts as compared to the base material spots (4, 5, 6). The spot EDS spectra corresponding to white spot region and parent material zone is provided in Fig. 20 (b,c).

As oxygen is a relatively lighter element, elemental detection errors are possible. On the contrary, Titanium always express high affinity

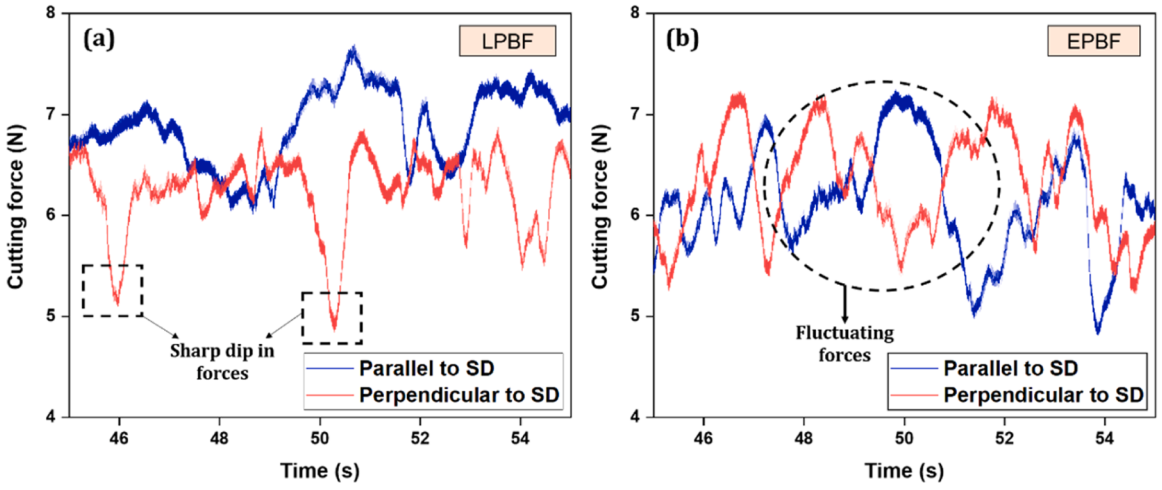

Fig. 15. Cutting force signals acquired during micro-cutting of (a) LPBF and (b) EPBF Ti-15Mo-5Zr-3Al alloy in directions parallel and perpendicular to beam scanning.

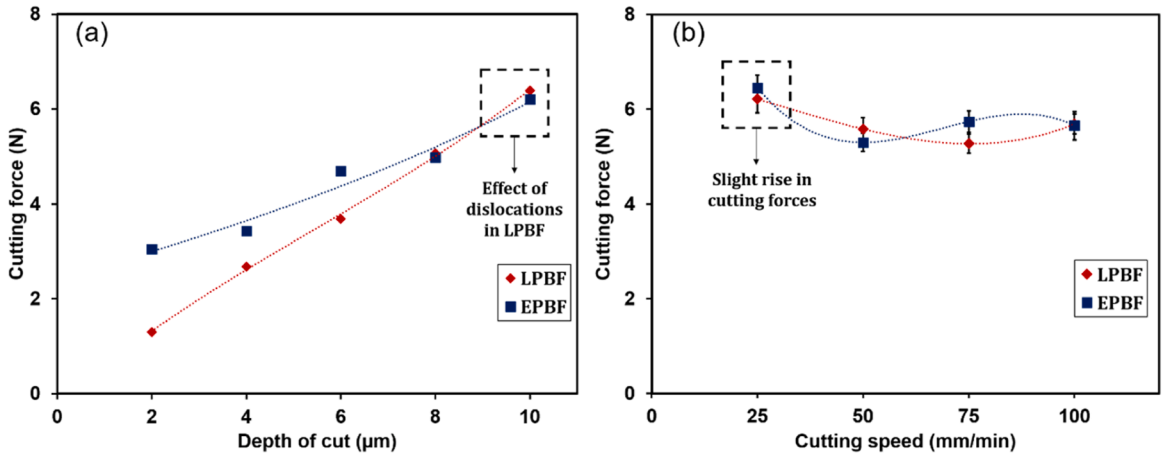

Fig. 16. Effect of (a) depth of cut and (b) cutting speed on LPBF and EPBF Ti alloy samples in UPDT.

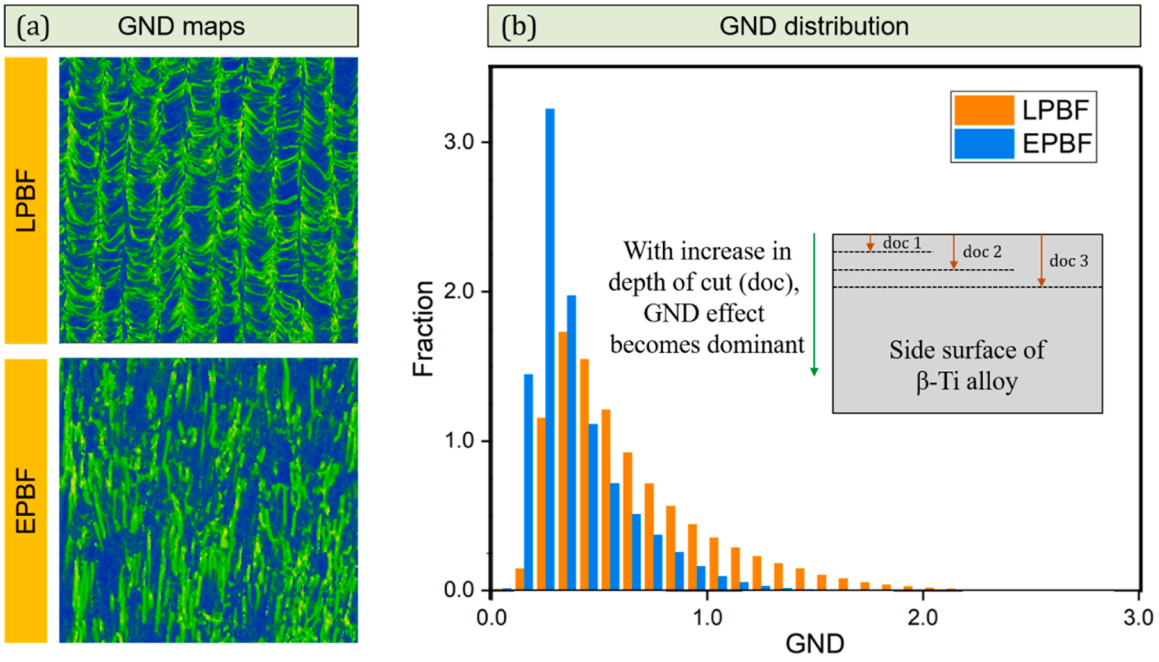

Fig. 17. Geometrically necessary dislocation (GND) data comprising (a) GND maps and (b) GND distribution corresponding to LPBF and EPBF samples.

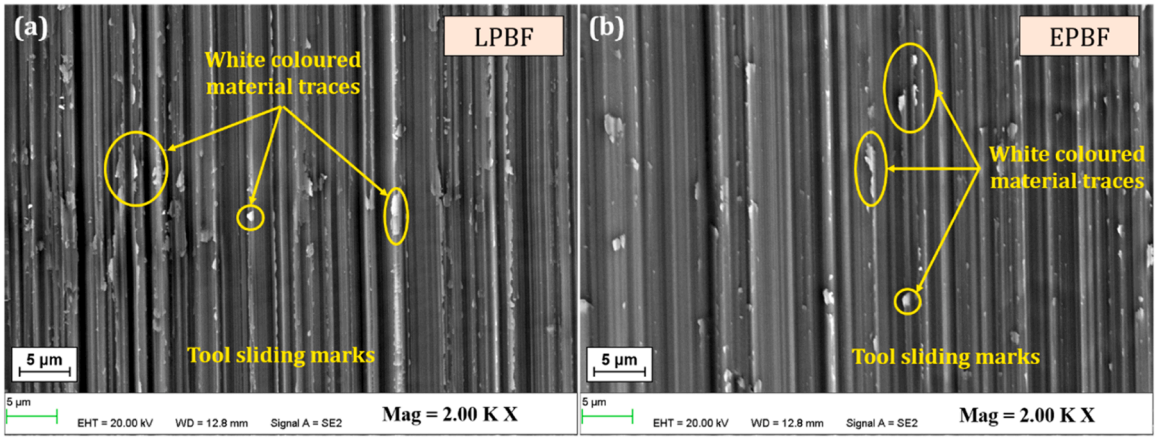

Fig. 18. SEM images representing the surfaces of micro-groove cut on (a) LPBF and (b) EPBF samples.

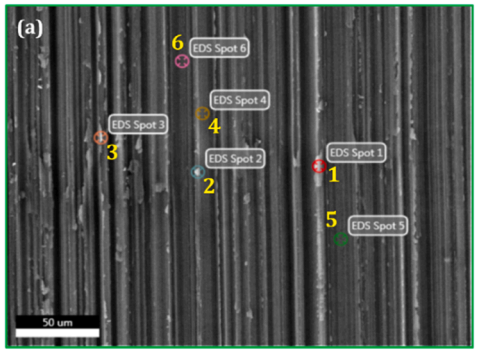

Region	Spot No	Oxygen weight percent (%)
White spot region	1	0
	2	1.70
	3	0
Dark region (Base material)	4	-
	5	-
	6	-

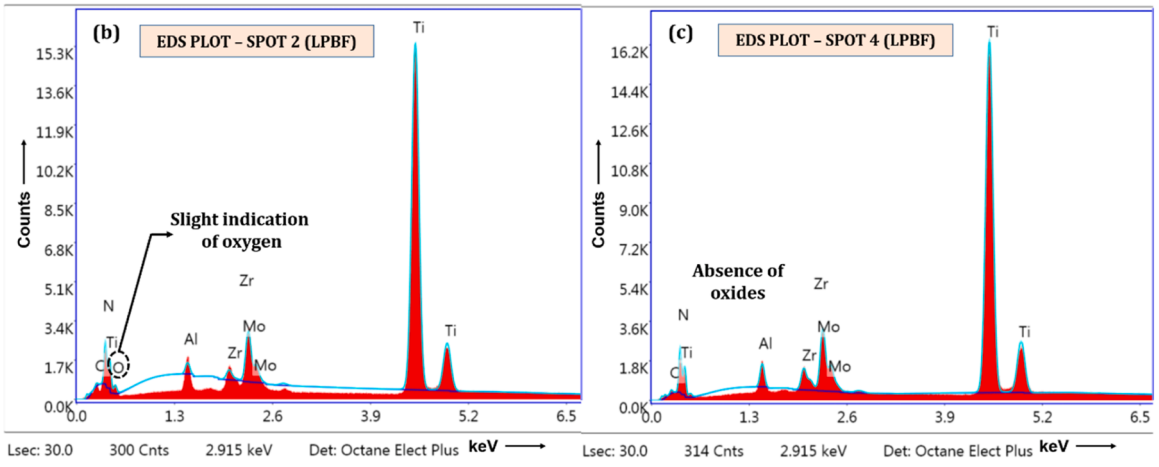

Fig. 19. (a) Microgroove cut on LPBF sample and spot EDS spectrum taken over (b) white spot region (spot 2) and (c) base material region (spot 4).

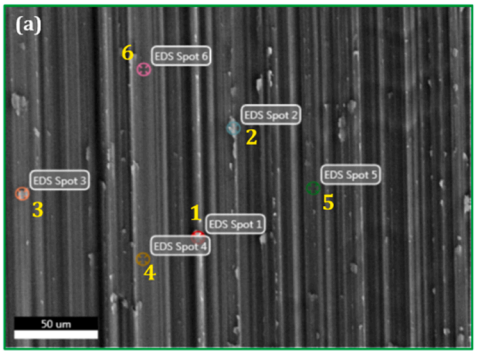

Region	Spot No	Oxygen weight percent (%)
White spot region	1	1.41
	2	1.50
	3	2.00
Dark region (Base material)	4	-
	5	-
	6	-

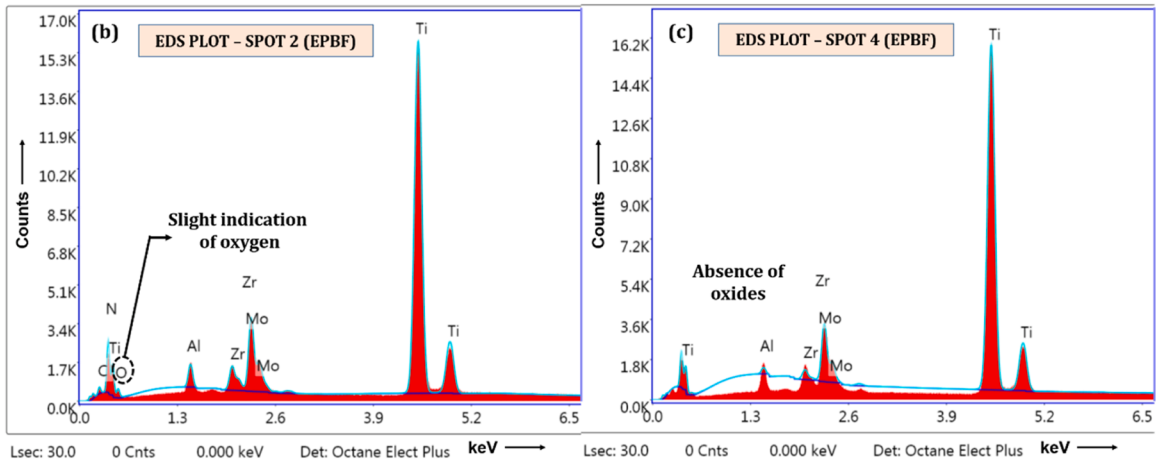

Fig. 20. (a) Microgroove cut on EPBF sample and spot EDS spectrum taken over (b) white spot region (spot 2) and (c) base material region (spot 4).

towards oxygen element. Thus, the weight percentage of oxygen obtained from EDS results, although minimal, require further verification. Hence, to confirm the reliability of obtained results, Raman spectroscopy was conducted at the white spots on UPDT surface corresponding to LPBF and EPBF samples. He-Ne laser having a wavelength of 633 nm was employed as the excitation source. Calibration of the equipment was done prior to the measurements using the 521 cm^{-1} Raman reference line of a Silicon (Si) wafer. An acquisition time of 30 s was fixed with 3 accumulations for obtaining the characteristic Raman spectra. The smoothened spectral profile (Savitzky-Golay smoothing) obtained from the white spots of both LPBF and EPBF alloys are provided in Fig. 21 (a, b).

Typically, the oxides of Ti in the form of Anatase phase will exhibit its characteristic peaks at 144 cm^{-1}, 197 cm^{-1}, 399 cm^{-1}, 513 cm^{-1} and 639 cm^{-1} [68]. Similarly, characteristic peaks related to Rutile phase will be present at 142 cm^{-1}, 236 cm^{-1}, 446 cm^{-1} and 610 cm^{-1}. However, only minimal changes are observed in the spectral intensity (counts), lacking any distinctive or significant peaks of oxygen in the spectra for both the samples. Thus, UPDT contributes to oxide free surfaces on β-Ti alloys after UPDT. In other words, the chemical composition of the Ti alloy surfaces remain unaffected after UPDT indicating the viability of the process in implant applications. The white colouration noticed in SEM images can be due to the minor height variations of deformed material relative to dark regions.

4.4.2. Characterization of LPBF and EPBF chips

The chip morphology study was carried out by collecting the micro-chips of LPBF and EPBF samples after each micro-cutting experiments to evaluate the ultra-precision cutting performance. Fig. 22 (a) and Fig. 22 (c) represent the FESEM morphologies of front and back side of the chip obtained from LPBF sample at a cutting velocity (v_c) of 50 mm/min and a depth of cut (doc) of 10 μm. As shown in Fig. 22 (a), while machining LPBF Ti-15Mo-5Zr-3Al alloy via UPDT, a chip exhibiting lamellar morphology with repeated serrations is formed indicating localized shearing of the material. The high degree of segmentation/serrations is responsible for the significant force variations experienced during micro-cutting as evident from Fig. 15. Due to the poor thermal conductivity of Ti alloy, the micro-cutting process develops competition between strain hardening and thermal softening thereby inducing thermoplastic shear instability [69,70]. Consequently, the cutting action causes the shear bands to promote chip segmentation. The free surface of the chip also contains adhered chip particles present earlier over the pre-machined surface. As visible from Fig. 22 (b), EPBF chip also exhibit serrations at regular intervals resembling lamellar structure with some regions having a narrow spacing between the consecutive serrations. Thus, the chip morphology observations of EPBF sample is similar to the morphology visible on LPBF chip.

The chip surface opposite to the free surface of chip (back side) represents the contact surface between the tool and chip during machining. From Fig. 22 (c,d), it is understood that irregularities are apparent on the tool-chip contact surface for both LPBF and EPBF alloys owing to the presence of PBF induced defects in the material. The major irregularities comprise of localized parent material adhesion and adherence of partially melted zones. The migration and adhesion of parent material towards chips occur from defect oriented regions characterized by inadequate material properties. The observations are similar for both LPBF and EPBF samples. The internal defects existing in the material exhibit poor bonding characteristics with the parent material. Moreover, the poor thermal conductivity of Ti alloy causes heat concentration at machining zone during deformation leading to localized thermal softening of the material. Thus, the defects embedded in the alloy material get adhered to the tool-chip contact surface during machining resulting in minor surface defects after UPDT. The results support the observations regarding machining induced surface defects as visible in the topographical images provided in Fig. 7.

4.5. Analysis of generated micro-features

Micro-texturing is extremely significant in biomedical implants as it plays a vital role in controlling cell growth, osseointegration and blood cell adhesion. The effectiveness of UPDT in producing precise micro-features over metal AM β-Ti samples was inspected to assess the process potential in enhancing implant functionality. A convex micro-lens array was chosen as the micro-feature in the study due to non-linearity in the profile and to effectively understand the dimensional deviations with respect to a curvature. The details related to tool path program generation and geometrical accuracy achieved by microlens on LPBF and EPBF β-Ti alloys are discussed in this section.

4.5.1. Program generation

The tool path program for micro-feature processing was generated using MATLAB software. The tool path was designed to follow a spiral trajectory across the metal AM surface at a constant feed rate. The successful tracing of co-ordinate points defined in the tool path is realized through the synchronized motion of linear (X and Z) and rotational (C) axes. The generation of micro-features is facilitated through the slow tool servo motion in Z axis. Constant angle method is used to discretize the rotational angle for each revolution in order to define the control points along the trajectory of tool. The coordinates in the NC program corresponding to tool path is defined based on the control points obtained through discretization. Microlens arrays were produced on both LPBF and EPBF samples by maintaining a microlens curvature (c) of 0.2 with radius of profile base (r) = 0.2 mm. The objective was to assess the extent of homogeneity in fabrication in response to the material specific attributes exhibited by the samples. The Z-axis coordinate values in the generated tool path is defined by Eq. 1 where k represents the conic coefficient (k = 0 for spherical surface).

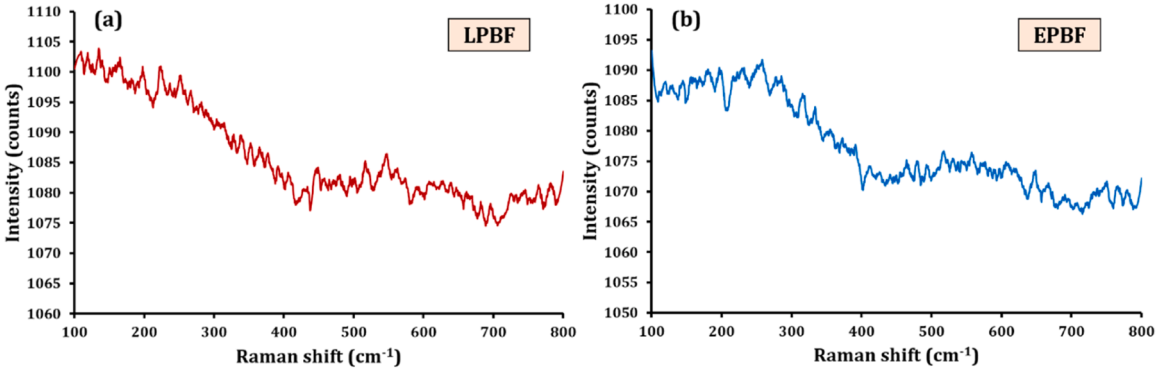

Fig. 21. Raman spectra obtained from the UPDT induced white spots corresponding to (a) LPBF and (b) EPBF sample surfaces.

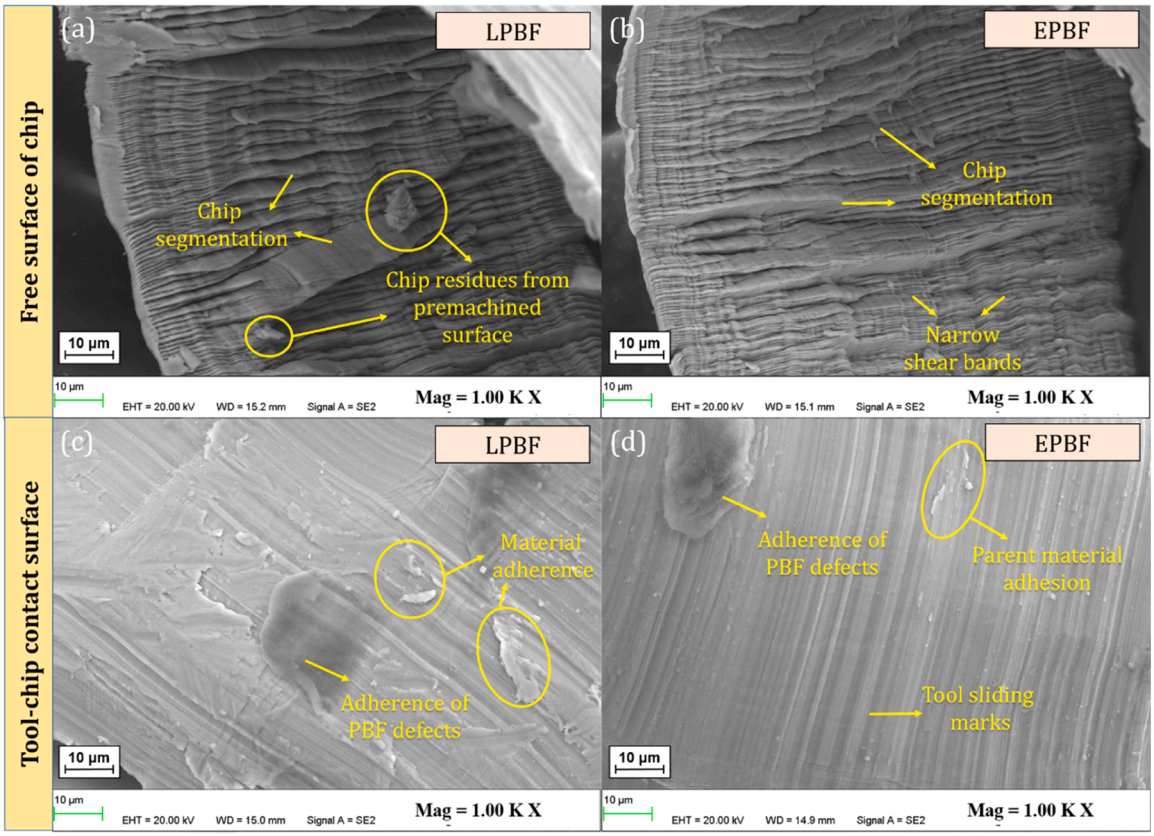

Fig. 22. FESEM morphologies of chips (front and back side of chip) obtained from (a,b) LPBF and (c,d) EPBF samples after UPDT micro-cutting experiments (v_c = 50 mm/min, doc = 10 µm).

$$Z(r) = \frac{cr^2}{1 + \sqrt{1 - (1+k)c^2r^2}} \quad (1)$$

The actual geometry of microlens array and a single microlens can be interpreted from the MATLAB images provided in Fig. 23 (a,b,c).

4.5.2. Surface topography and profile analysis

A single microlens among the generated array was chosen for evaluating the potential of UPDT in microfeature generation. A non-contact optical profilometer was used to capture the surface topography associated with the microlens. The 2D and 3D topographical images of the microlens produced on LPBF and EPBF samples can be seen from Fig. 24 (a, c) and Fig. 24 (b, d) respectively. It can be observed that both the samples generate microlens with a convex profile nearly resembling the MATLAB design. The dimensional deviations of the convex microlens is quantified by scanning the geometrical lens profile for both samples using non-contact optical profilometer.

Fig. 25 establishes that the microlens generated on both samples follows a profile nearly identical to the designed profile indicating the promising potential of UPDT process. However, dimensional deviations in nanometric range can be observed on the UPDT generated microlens. Such deviations occur due to the material adhesion and defect migration towards chip surfaces as identified from the chip morphology discussed in Section 4.4.2. Therefore, appropriate selection of PBF parameters is inevitable to hinder the defect formation in printed samples so as to obtain dimensionally accurate microfeatures.

Further, EPBF microlens exhibit comparatively larger dimensional deviations relative to LPBF microlens. The reason can be due to the irregularities evolved over EPBF microlens surface during UPDT process as evident from the FESEM image in Fig. 25 (b). The surface of EPBF

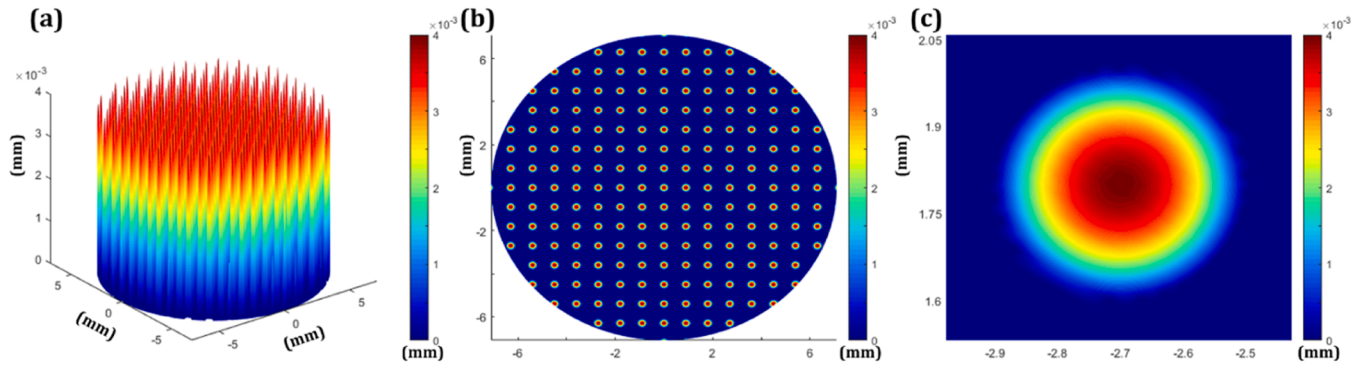

Fig. 23. MATLAB design of convex microlens array in (a) 3D, (b) 2D and image for a (c) single convex microlens (Radius of a single microlens = 0.2 mm, microlens curvature (r) = 0.2 and height of each microlens in the generated array = 4 µm).

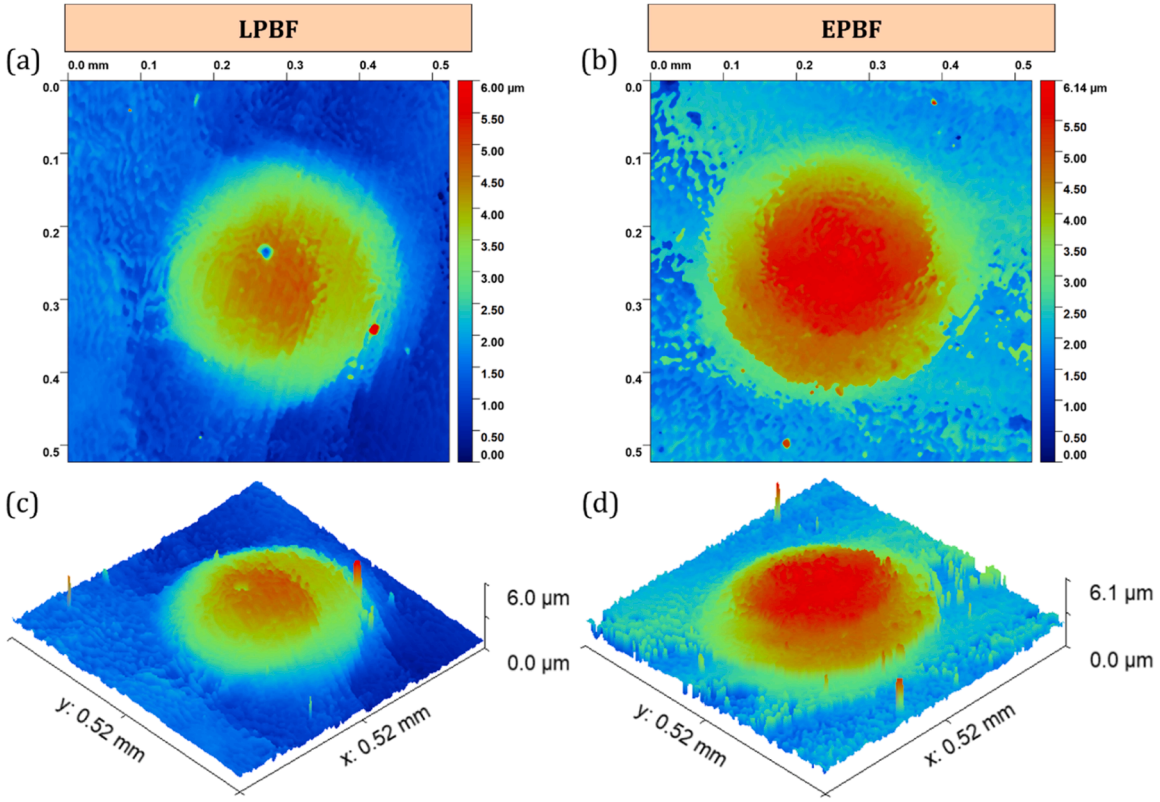

Fig. 24. 2D and 3D topographical images of microlens obtained after UPDT on (a,c) LPBF and (b,d) EPBF samples.

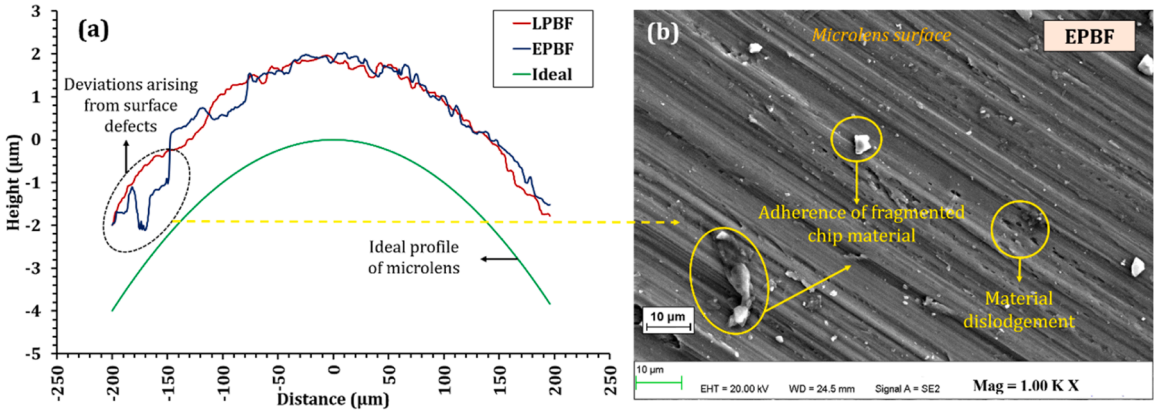

Fig. 25. (a) Geometrical profile of convex microlens (designed and actual) generated after UPDT on PBF samples and (b) surface irregularities responsible for dimensional deviations in EPBF samples.

microlens exhibits the presence of many fragmented chips which has undergone adhesion during UPDT. Such defects can affect the profile dimensions at arbitrary positions as visible in Fig. 25 (a). Moreover, material dislodgement resulting from cutting action is apparent in EPBF samples leading to deviations from actual dimensions. During micro-texturing, the presence of relatively harder α-precipitates in β dominant alloy can trigger material dislodgement from microlens surface resulting in the formation of small pit/porous zones thereby aggravating dimensional accuracy. Thus, LPBF samples demonstrate a profile accuracy closer to ideal profile relative to EPBF samples.

5. Conclusions

The present investigation explored the potential of ultra-precision diamond turning in the surface post-treatment of metal additive manufactured beta-Titanium alloy used in biomedical applications. The study discusses the surface integrity, process performance and micro-feature accuracy aspects by taking into consideration the difference in material specific characteristics induced by laser and electron beam thermal sources. The following conclusions can be derived from the present study:

1. The adoption of UPDT process transforms the higher as-built surface roughness into nano-level surface finish of ~66.3 nm and ~104.3 nm respectively on LPBF and EPBF samples.
2. Preheating in EPBF induces alpha phase formation in the form of plate like precipitates in EPBF Ti-15Mo-5Zr-3A alloy and is

responsible for the slightly higher hardness (~365 HV) relative to LPBF alloy (~344 HV).
3. The interaction of cutting tool with scan track boundaries leads to sharp dip in forces in UPDT micro-cutting of LPBF samples. On the other side, the interaction of cutting tool with grain boundaries are dominant in EPBF process resulting in fluctuating forces during UPDT irrespective of the scan direction.
4. Marginal increase in depth of cut is found to significantly influence the trend in cutting force variation associated with LPBF and EPBF samples. Moreover, oxide-free surfaces can be obtained on Ti alloy surfaces after UPDT indicating negligible modification in surface composition.
5. Lamellar-like chip morphology with serrations/segmentation is observed on the chips obtained from LPBF and EPBF samples after UPDT. Adhesion of parent material and powder bed fusion induced defects also occur at the tool-chip contact surface of chip.
6. Precise microfeatures can be successfully fabricated on metal AM samples through UPDT, with minimal dimensional deviations on LPBF samples, thereby confirming the potential of the process in biomedical implant applications.

In a nutshell, UPDT process shows promising potential in extending the acceptability of additively manufactured β-Titanium alloys in bio-implant applications. LPBF samples exhibit more efficacy than EPBF samples in terms of better surface finish and dimensional accuracy. The present study opens diverse research areas which can enhance the wide scale adoption of the process in implant applications. The reference setting and discretization of intricate microfeatures remain as a critical issue in UPDT processing of freeform AM surfaces. In such a context, the generation of tool path design demands competitive approaches. Similarly, the effect of PBF parameters on UPDT performance can be investigated to ultimately yield an optimal quality defect-free product satisfying biomedical standards. Moreover, a detailed assessment of post-treated implant focussed on cell growth characteristics, blood cell adhesion, bone tissue compatibility etc. needs to be inspected to determine the degree of biocompatibility. Further, exploring the effect of sample heat treatment stands as a forward-looking investigation as it may contribute to microstructural homogeneity in the alloy and promising outcomes after UPDT.

CRediT authorship contribution statement

Jibin Boban: Writing – original draft, Visualization, Validation, Software, Methodology, Investigation, Formal analysis, Data curation, Conceptualization. **Afzaal Ahmed:** Writing – review & editing, Visualization, Validation, Supervision, Conceptualization. **Ozkan Gokcekaya:** Writing – review & editing, Validation, Supervision, Resources. **Takayoshi Nakano:** Writing – review & editing, Resources.

Declaration of Competing Interest

No conflict of interest.

Acknowledgement

The authors would like to acknowledge the support received for the project from Industry Collaboration and Sponsored Research (ICSR) section of IIT Palakkad (Ref No: IITPKD/ICSR/REC/2023/109). The authors are also grateful for the consistent support received from the staff in Central Instrumentation Facility (CIF) and Design & Manufacturing (D & M) Laboratory at IIT Palakkad, India.

References

[1] Abdulhameed O, Al-Ahmari A, Ameen W, Mian SH. Additive manufacturing: challenges, trends, and applications. Adv Mech Eng 2019;11(2):1–27. https://doi.org/10.1177/1687814018822880.
[2] Ngo TD, Kashani A, Imbalzano G, Nguyen KTQ, Hui D. Additive manufacturing (3D printing): a review of materials, methods, applications and challenges. Compos, Part B 2018;143:172–96. https://doi.org/10.1016/j.compositesb.2018.02.012.
[3] Najmon JC, Raeisi S, Tovar A. 2 - Review of additive manufacturing technologies and applications in the aerospace industry. In: Froes F, Boyer R, editors. Additive Manufacturing for the Aerospace Industry. Elsevier; 2019. p. 7–31.
[4] Boban J, Ahmed A. Electric discharge aided surface post-treatment of laser powder bed fused non-planar metallic components for enhanced form accuracy. J Manuf Process 2024;109:564–82. https://doi.org/10.1016/j.jmapro.2023.12.028.
[5] Abhilash PM, Ahmed A. An image-processing approach for polishing metal additive manufactured components to improve the dimensional accuracy and surface integrity. Int J Adv Manuf Technol 2023;125(7):3363–83. https://doi.org/10.1007/s00170-023-10916-1.
[6] Anand M, Das AK. Issues in fabrication of 3D components through DMLS Technique: a review. Opt Laser Technol 2021;139:106914. https://doi.org/10.1016/j.optlastec.2021.106914.
[7] Calignano F, Lorusso M, Pakkanen J, Trevisan F, Ambrosio EP, Manfredi D, et al. Investigation of accuracy and dimensional limits of part produced in aluminum alloy by selective laser melting. Int J Adv Manuf Technol 2017;88(1):451–8. https://doi.org/10.1007/s00170-016-8788-9.
[8] J. Boban, P. Abhilash, A. Ahmed, Post-processing of additively manufactured metallic bioimplants: Approaches, challenges and future trends, in: P. Abhilash, K. K. Gajrani, X. Luo (Eds.), Bioimplants Manufacturing: Fundamentals and Advances 2024, p. 206.
[9] Rajput AS, Kapil S, Das M. A post processing technique to achieve nanofinishing for functionality enhancement of Ti-6Al-4V femoral head fabricated by Laser Powder Bed Fusion. CIRP J Manuf Sci Technol 2023;45:99–112. https://doi.org/10.1016/j.cirpj.2023.06.006.
[10] Jain VK. Nanofinishing science and technology: basic and advanced finishing and polishing processes. CRC Press,; 2016.
[11] Kumar M, Kumar A, Yadav HNS, Alok A, Das M. Abrasive based finishing method applied on biomedical implants: A review. Mater Today: Proc 2021;47:3985–92. https://doi.org/10.1016/j.matpr.2021.04.137.
[12] Zhang Y, Fan Z, Xing Y, Jia S, Mo Z, Gong H. Effect of microtopography on osseointegration of implantable biomaterials and its modification strategies. Front Bioeng Biotechnol 2022;10:981062. https://doi.org/10.3389/fbioe.2022.981062.
[13] Boban J, Abhilash PM, Ahmed A, Rahman MA. 10.11 - An overview on post-processing of metal additive manufactured components. In: Hashmi S, editor. Comprehensive Materials Processing (Second Edition). Oxford: Elsevier; 2024. p. 231–70.
[14] Boban J, Deshmukh SM, Ahmed A. Ultra-precision surface finishing and feature generation on metal additive manufactured components with controlled tool path design. Procedia CIRP 2023;119:450–5. https://doi.org/10.1016/j.procir.2023.03.108.
[15] Boban J, Ahmed A. Effect of material composition on the action of surface active medium in ultra-precision microcutting. Procedia CIRP 2024;123:244–9. https://doi.org/10.1016/j.procir.2024.05.044.
[16] Tauhiduzzaman M, Veldhuis SC. Effect of material microstructure and tool geometry on surface generation in single point diamond turning. Precis Eng 2014;38(3):481–91. https://doi.org/10.1016/j.precisioneng.2014.01.002.
[17] Hashmi AW, Mali HS, Meena A, Saxena KK, Ahmad S, Agrawal MK, et al. A comprehensive review on surface post-treatments for freeform surfaces of bio-implants. J Mater Res Technol 2023;23:4866–908. https://doi.org/10.1016/j.jmrt.2023.02.007.
[18] Zhang Y, Li J, Che S, Yang Z, Tian Y. Chemical leveling mechanism and oxide film properties of additively manufactured Ti–6Al–4V alloy. J Mater Sci 2019;54(21):13753–66. https://doi.org/10.1007/s10853-019-03855-4.
[19] Wysocki B, Idaszek J, Buhagiar J, Szlązak K, Brynk T, Kurzydłowski KJ, et al. The influence of chemical polishing of titanium scaffolds on their mechanical strength and in-vitro cell response. Mater Sci Eng, C 2019;95:428–39. https://doi.org/10.1016/j.msec.2018.04.019.
[20] Bezuidenhout M, Ter Haar G, Becker T, Rudolph S, Damm O, Sacks N. The effect of HF-HNO3 chemical polishing on the surface roughness and fatigue life of laser powder bed fusion produced Ti6Al4V. Mater Today Commun 2020;25:101396. https://doi.org/10.1016/j.mtcomm.2020.101396.
[21] Scherillo F, Manco E, Hassanin AE, Franchitti S, Pirozzi C, Borrelli R. Chemical surface finishing of electron beam melted Ti6Al4V using HF-HNO3 solutions. J Manuf Process 2020;60:400–9. https://doi.org/10.1016/j.jmapro.2020.10.033.
[22] Sefer B, Dobryden I, Almqvist N, Pederson R, Antti M-L. Chemical Milling of Cast Ti-6Al-4V and Ti-6Al-2Sn-4Zr-2Mo Alloys in Hydrofluoric-Nitric Acid Solutions. Corrosion 2016;73(4):394–407. https://doi.org/10.5006/2277.
[23] Jain S, Corliss M, Tai B, Hung WN. Electrochemical polishing of selective laser melted Inconel 718. Procedia Manuf 2019;34:239–46. https://doi.org/10.1016/j.promfg.2019.06.145.
[24] Larsson C, Thomsen P, Lausmaa J, Rodahl M, Kasemo B, Ericson LE. Bone response to surface modified titanium implants: studies on electropolished implants with different oxide thicknesses and morphology. Biomaterials 1994;15(13):1062–74. https://doi.org/10.1016/0142-9612(94)90092-2.
[25] Marimuthu S, Triantaphyllou A, Antar M, Wimpenny D, Morton H, Beard M. Laser polishing of selective laser melted components. Int J Mach Tools Manuf 2015;95:97–104. https://doi.org/10.1016/j.ijmachtools.2015.05.002.

[26] Li C, Liu D, Liu G, Liu S, Jin X, Bai Y. Surface characteristics enhancement and morphology evolution of selective-laser-melting (SLM) fabricated stainless steel 316L by laser polishing. Opt Laser Technol 2023;162:109246. https://doi.org/10.1016/j.optlastec.2023.109246.
[27] Yung KC, Wang WJ, Xiao TY, Choy HS, Mo XY, Zhang SS, et al. Laser polishing of additive manufactured CoCr components for controlling their wettability characteristics. Surf Coat Technol 2018;351:89–98. https://doi.org/10.1016/j.surfcoat.2018.07.030.
[28] Zhou J, Liao C, Shen H, Ding X. Surface and property characterization of laser polished Ti6Al4V. Surf Coat Technol 2019;380:125016. https://doi.org/10.1016/j.surfcoat.2019.125016.
[29] Gora WS, Tian Y, Cabo AP, Ardron M, Maier RR, Prangnell P, et al. Enhancing surface finish of additively manufactured titanium and cobalt chrome elements using laser based finishing. Phys Procedia 2016;83:258–63. https://doi.org/10.1016/j.phpro.2016.08.021.
[30] Tian Y, Gora WS, Cabo AP, Parimi LL, Hand DP, Tammas-Williams S, et al. Material interactions in laser polishing powder bed additive manufactured Ti6Al4V components. Addit Manuf 2018;20:11–22. https://doi.org/10.1016/j.addma.2017.12.010.
[31] Ma C, Guan Y, Zhou W. Laser polishing of additive manufactured Ti alloys. Opt Lasers Eng 2017;93:171–7. https://doi.org/10.1016/j.optlaseng.2017.02.005.
[32] Xu Z, Ouyang W, Liu Y, Jiao J, Liu Y, Zhang W. Effects of laser polishing on surface morphology and mechanical properties of additive manufactured TiAl components. J Manuf Process 2021;65:51–9. https://doi.org/10.1016/j.jmapro.2021.03.014.
[33] Boban J, Ahmed A, Jithinraj EK, Rahman MA, Rahman M. Polishing of additive manufactured metallic components: retrospect on existing methods and future prospects. Int J Adv Manuf Technol 2022;121:83–125. https://doi.org/10.1007/s00170-022-09382-y.
[34] Boban J, Ahmed A. Defect mitigation and surface enhancement of additively manufactured AlSi10Mg internal features using electro-thermal post-treatment. Mater Lett 2023;353:135267. https://doi.org/10.1016/j.matlet.2023.135267.
[35] Ermergen T, Taylan F. Review on surface quality improvement of additively manufactured metals by laser polishing. Arab J Sci Eng 2021;46(8):7125–41. https://doi.org/10.1007/s13369-021-05658-9.
[36] Bouland C, Urlea V, Beaubier K, Samoilenko M, Brailovski V. Abrasive flow machining of laser powder bed-fused parts: numerical modeling and experimental validation. J Mater Process Technol 2019;273:116262. https://doi.org/10.1016/j.jmatprotec.2019.116262.
[37] Uhlmann E, Roßkamp S. Surface integrity and chip formation in abrasive flow machining. Procedia CIRP 2018;71:446–52. https://doi.org/10.1016/j.procir.2018.05.048.
[38] Zhang J, Chaudhari A, Wang H. Surface quality and material removal in magnetic abrasive finishing of selective laser melted 316L stainless steel. J Manuf Process 2019;45:710–9. https://doi.org/10.1016/j.jmapro.2019.07.044.
[39] Boban J, Ahmed A. Improving the surface integrity and mechanical properties of additive manufactured stainless steel components by wire electrical discharge polishing. J Mater Process Technol 2021;291:117013. https://doi.org/10.1016/j.jmatprotec.2020.117013.
[40] Boban J, Ahmed A. Electric discharge assisted post-processing performance of high strength-to-weight ratio alloys fabricated using metal additive manufacturing. CIRP J Manuf Sci Technol 2022;39:159–74. https://doi.org/10.1016/j.cirpj.2022.08.002.
[41] Boban J, Ahmed A. Finishing the surface micro-layer of additively manufactured TiAl alloy using electro-thermal discharge assisted post-processing. J Micro 2023;6(2):151–61. https://doi.org/10.1177/25165984231151745.
[42] Bagehorn S, Wehr J, Maier H. Application of mechanical surface finishing processes for roughness reduction and fatigue improvement of additively manufactured Ti-6Al-4V parts. Int J Fatigue 2017;102:135–42. https://doi.org/10.1016/j.ijfatigue.2017.05.008.
[43] Rakurty CS, M. K, Bowser B, Rangasamy N, Kakaraparthi S, Dippolito R, et al. Grinding EB-PBF based additive manufactured Ti6Al4V: a surface integrity study. Adv Ind Manuf Eng 2023;7:100131. https://doi.org/10.1016/j.aime.2023.100131.
[44] Yan C, Hao L, Hussein A, Young P. Ti–6Al–4V triply periodic minimal surface structures for bone implants fabricated via selective laser melting. J Mech Behav Biomed Mater 2015;51:61–73. https://doi.org/10.1016/j.jmbbm.2015.06.024.
[45] Singla AK, Banerjee M, Sharma A, Singh J, Bansal A, Gupta MK, et al. Selective laser melting of Ti6Al4V alloy: Process parameters, defects and post-treatments. J Manuf Process 2021;64:161–87. https://doi.org/10.1016/j.jmapro.2021.01.009.
[46] Kaynak Y, Kitay O. The effect of post-processing operations on surface characteristics of 316L stainless steel produced by selective laser melting. Addit Manuf 2019;26:84–93. https://doi.org/10.1016/j.addma.2018.12.021.
[47] Sun Y, Bailey R, Moroz A. Surface finish and properties enhancement of selective laser melted 316L stainless steel by surface mechanical attrition treatment. Surf Coat Technol 2019;378:124993. https://doi.org/10.1016/j.surfcoat.2019.124993.
[48] Portella Q, Chemkhi M, Retraint D. Influence of surface mechanical attrition treatment (SMAT) post-treatment on microstructural, mechanical and tensile behaviour of additive manufactured AISI 316L. Mater Charact 2020;167:110463. https://doi.org/10.1016/j.matchar.2020.110463.
[49] Arifvianto B, Suyitno, Mahardika M. Effects of surface mechanical attrition treatment (SMAT) on a rough surface of AISI 316L stainless steel. Appl Surf Sci 2012;258(10):4538–43. https://doi.org/10.1016/j.apsusc.2012.01.021.
[50] Worts N, Jones J, Squier J. Surface structure modification of additively manufactured titanium components via femtosecond laser micromachining. Opt Commun 2019;430:352–7. https://doi.org/10.1016/j.optcom.2018.08.055.
[51] Nagarajan B, Hu Z, Song X, Zhai W, Wei J. Development of micro selective laser melting: the state of the art and future perspectives. Engineering 2019;5(4):702–20. https://doi.org/10.1016/j.eng.2019.07.002.
[52] Rogkas N, Vakouftsis C, Spitas V, Lagaros ND, Georgantzinos SK. Design aspects of additive manufacturing at microscale: a review. Micromachines 2022;13(5). https://doi.org/10.3390/mi13050775.
[53] Simson D, Subbu SK. Investigation of build strategies for microfeatures fabrication using laser powder bed fusion. J Manuf Process 2022;79:990–1002. https://doi.org/10.1016/j.jmapro.2022.05.042.
[54] Mekhiel S, Koshy P, Elbestawi MA. Additive texturing of metallic surfaces for wetting control. Addit Manuf 2021;37:101631. https://doi.org/10.1016/j.addma.2020.101631.
[55] Dwivedi S, Dixit AR, Das AK, Adamczuk K. Additive texturing of metallic implant surfaces for improved wetting and biotribological performance. J Mater Res Technol 2022;20:2650–67. https://doi.org/10.1016/j.jmrt.2022.08.029.
[56] Wei W, Pingmei M, Xinmin Z, Xinchao L, Yunyan Z, Shen N, et al. Additive manufacturing of three-dimensional intricate microfeatures by electrolyte-column localized electrochemical deposition. Addit Manuf 2022;50:102582. https://doi.org/10.1016/j.addma.2021.102582.
[57] Neo DWK. Ultraprecision machining of hybrid freeform surfaces using multiple-axis diamond turning. Springer,; 2017.
[58] Gong H, Wang Y, Song L, Fang FZ. Spiral tool path generation for diamond turning optical freeform surfaces of quasi-revolution. Comput-Aided Des 2015;59:15–22. https://doi.org/10.1016/j.cad.2014.08.001.
[59] Azmat A, Asrar S, Channa IA, Ashfaq J, Ali Chandio I, Chandio AD, et al. Comparative study of biocompatible titanium alloys containing non-toxic elements for orthopedic implants. Crystals 2023.
[60] Abd-Elaziem W, Darwish MA, Hamada A, Daoush WM. Titanium-Based alloys and composites for orthopedic implants applications: a comprehensive review. Mater Des 2024;241:112850. https://doi.org/10.1016/j.matdes.2024.112850.
[61] Lee SH, Todai M, Tane M, Hagihara K, Nakajima H, Nakano T. Biocompatible low Young's modulus achieved by strong crystallographic elastic anisotropy in Ti–15Mo–5Zr–3Al alloy single crystal. J Mech Behav Biomed Mater 2012;14:48–54. https://doi.org/10.1016/j.jmbbm.2012.05.005.
[62] Zhang L-C, Chen L-Y, Zhou S, Luo Z. Powder bed fusion manufacturing of beta-type titanium alloys for biomedical implant applications: a review. J Alloy Compd 2023;936:168099. https://doi.org/10.1016/j.jallcom.2022.168099.
[63] Sun S-H, Hagihara K, Ishimoto T, Suganuma R, Xue Y-F, Nakano T. Comparison of microstructure, crystallographic texture, and mechanical properties in Ti–15Mo–5Zr–3Al alloys fabricated via electron and laser beam powder bed fusion technologies. Addit Manuf 2021;47:102329. https://doi.org/10.1016/j.addma.2021.102329.
[64] Ibrahim P, Garrard R, Attallah MM. Laser powder bed fusion of a β titanium alloy: microstructural development, post-processing, and mechanical behaviour. Mater Sci Eng, A 2024;905:146617. https://doi.org/10.1016/j.msea.2024.146617.
[65] Zhao X, Li S, Zhang M, Liu Y, Sercombe TB, Wang S, et al. Comparison of the microstructures and mechanical properties of Ti–6Al–4V fabricated by selective laser melting and electron beam melting. Mater Des 2016;95:21–31. https://doi.org/10.1016/j.matdes.2015.12.135.
[66] Zhang C, Zhu J, Zheng H, Li H, Liu S, Cheng GJ. A review on microstructures and properties of high entropy alloys manufactured by selective laser melting. Int J Extrem Manuf 2020;2(3):032003. https://doi.org/10.1088/2631-7990/ab9ead.
[67] Heidarzadeh A, Mohammadzadeh R, Jafarian HR, Pruncu CI, Simar A. Role of geometrically necessary dislocations on mechanical properties of friction stir welded single-phase copper with medium stacking fault energy. J Mater Res Technol 2022;16:194–200. https://doi.org/10.1016/j.jmrt.2021.11.162.
[68] Duarte LT, Bolfarini C, Biaggio SR, Rocha-Filho RC, Nascente PAP. Growth of aluminum-free porous oxide layers on titanium and its alloys Ti-6Al-4V and Ti-6Al-7Nb by micro-arc oxidation. Mater Sci Eng, C 2014;41:343–8. https://doi.org/10.1016/j.msec.2014.04.068.
[69] Guan XR, Chen Q, Qu SJ, Cao GJ, Wang H, Feng AH, et al. Adiabatic shear instability in a titanium alloy: extreme deformation-induced phase transformation, nanotwinning, and grain refinement. J Mater Sci Technol 2023;150:104–13. https://doi.org/10.1016/j.jmst.2022.11.047.
[70] Komanduri R, Hou Z-B. On thermoplastic shear instability in the machining of a titanium alloy (Ti-6Al-4V). Metall Mater Trans A 2002;33(9):2995–3010. https://doi.org/10.1007/s11661-002-0284-1.